Scholars Journal of Engineering and Technology

OPEN ACCESS

Abbreviated Key Title: Sch J Eng Tech
ISSN 2347-9523 (Print) | ISSN 2321-435X (Online)
Journal homepage: https://saspublishers.com

Comprehensive Fluid Dynamics Analysis of Supersonic Jets impinging on Deflector Surface of Space Vehicles

R. C. Mehta[1*]

[1]Department of Aeronautical Engineering, Noorul Islam Centre for Higher Education, Kumaracoil 629180 India

DOI: https://doi.org/10.36347/sjet.2026.v14i02.003 | **Received:** 28.12.2025 | **Accepted:** 11.02.2026 | **Published:** 13.02.2026

***Corresponding author:** R. C. Mehta
Department of Aeronautical Engineering, Noorul Islam Centre for Higher Education, Kumaracoil 629180 India

Abstract | **Original Research Article**

Comprehensive flowfield study of supersonic jets impinging over a double-wedge deflector and an inclined plate and has been carried out by solving computational fluid dynamics (CFD) method and analytical method based on oblique shock relations. Three-dimensional compressible inviscid equations are solved employing finite volume methods using a multistage Runge-Kutta time stepping scheme. The numerical simulation is carried out for M_e = 2.2 and 3.1, T_e = 152°K, 266°K and 1811°K, p_e/p_e = 1.2, 0.8 and 0.6 and X_w/D_e = 3, 4 and 5. The supersonic jets emanating from a convergent-divergent nozzle impinging on a jet deflector can be customarily characterized by many flow discontinuities such as reflected shock, oblique shock, Mach disc, slip line, wedge shock and wall jet boundaries. The CFD results consist of pressure, density, Mach and temperature contour and surface pressure distributions. Influence of nozzle operating pressure ratio and nozzle exit temperature on the flowfield have been investigated using CFD analysis and compared with the experimental data of hot test cases of a solid rocket motor. On the base of space vehicle induced recirculation region is observed in the CFD simulation. The main focus of the present paper is to numerically analyze cold and hot jets and to investigate the effect of ratio of specific heats on flowfield of a double-wedge deflector. The numerical results are compared with the available experimental data and exhibit agreement between them. The numerical analysis will be useful for the selection of appropriate jet deflector during the lift-off phase of a space vehicle.

Keywords: Inviscid flow; Mach disc; Numerical analysis; Recirculation flow; Supersonic flow; Shock wave; Impinging jets; Inclined and double-wedge deflector.

INTRODUCTION

According to the main supersonic jet direction, deflectors could be divided into a single sided or a multi sided deflector. Different types of deflector surface generate different type pressure, acoustic efficiency [1] and thermal loads that may affect space vehicle as well as launch pad. The aspects to be considered for selection of deflector are to spread exhaust gases away from the launch pad through suitable deflector surfaces. It is generally known that the shape of the deflector surface is the major factor affecting the diversion performance of the jet deflector. Large space vehicles are commonly launched from a launch pad which include service structure, launch platform and a double-wedge deflector system as depicted in Fig. 1 with typical space vehicle. The launch platform lies beneath of the space vehicle with cutouts at some specific locations. The exhaust gases pass through these cutouts, impinges onto the deflector and deflects exhaust gases away from the vehicle. It is considered jet interaction with the launch pad an important and complex fluid dynamic problem during the lift-off of a launch vehicle. During rocket launching, the exhaust gas impingement induces large aerothermodynamic and aeroacoustic loads on the launch platform. To reduce the effect of thermal shock and dynamic of the nozzle jet flow, deflectors have been installed under the rocket engine to guide the exhaust gas of high temperature and velocity away from the channel minimum induced recirculation region. It is generally known that the shape of the deflector surface is the main factor affecting the diversion performance of the jet deflector. The deflector structure should be designed to restrain the exhaust jets from backdraft inside the deflector and to protect the rocket from damage of discharged exhaust gas during launching. The poor efficiency of diversion can cause blockage of the deflector channel by the recirculation flow. The accumulation and reflection of the high temperature gas have a negative influence on the stability of the jet deflector and security of the launch process. Using the

reasonable shape of the jet deflector can reduce the adverse effects caused by the induced recirculation of rocket exhaust gas. For these reasons, studying the diversion efficiency of different shapes of flame deflector is important for the safety of launch.

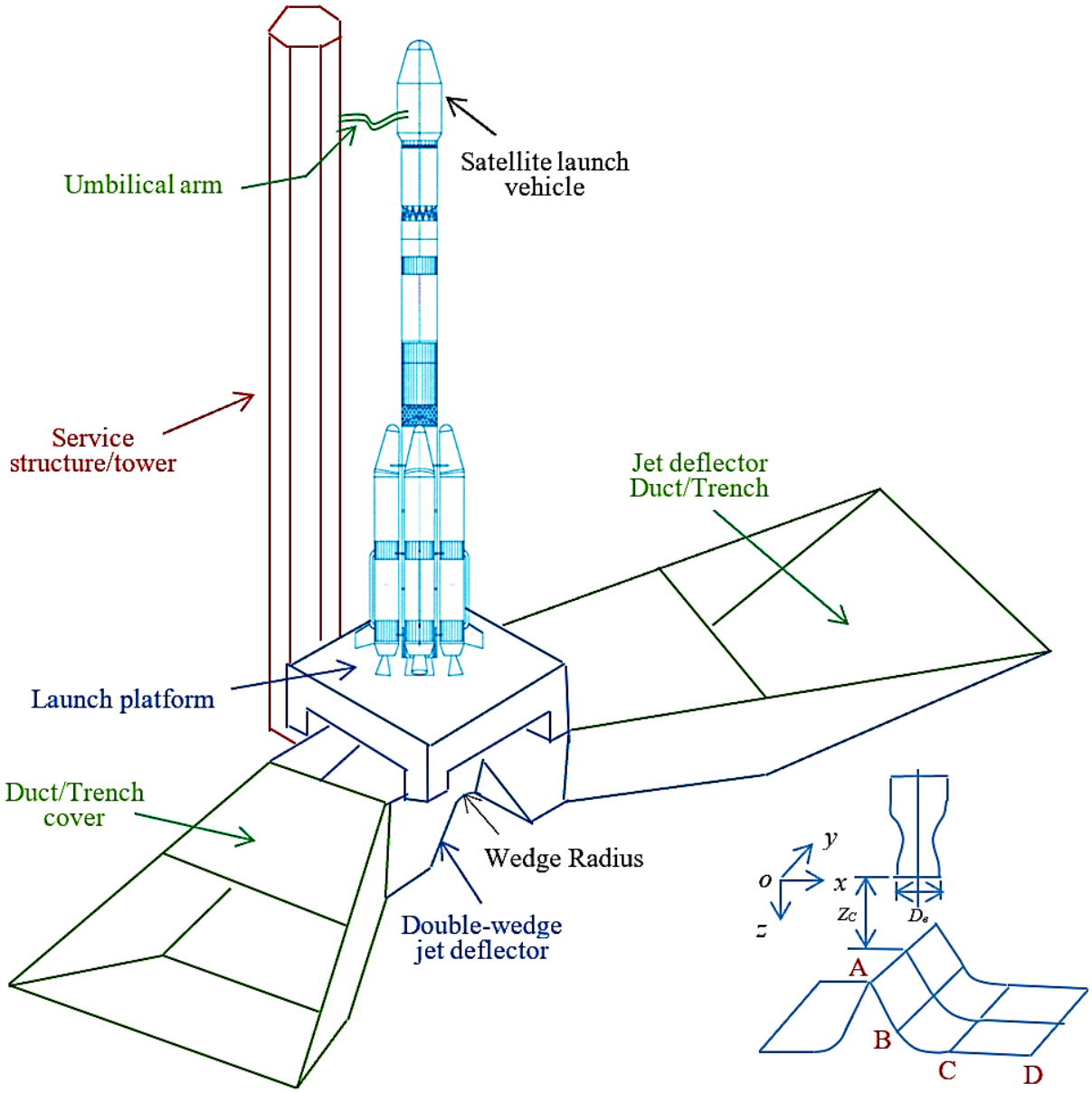

Fig. 1 Schematic sketch of a double-wedge deflector along with typical satellite launch vehicle

Recent launch of Soyuz MS 28 was successful but the launch pad in Baikonur (Kazakhstan) lost a critical piece of hardware [2]. Wedge-shaped deflector [3] (launch complex 34 for Saturn vehicle) was formed by joining together a two-unidirectional deflector. Sub-scale static tests conducted by NASA on a double wedge deflector for Saturn booster (T_o = 3572°K, T_e = 1811°K, M_e = 3.12 and γ = 1.2). Office National d'Etudes et de Recherches Aèropatialales (ONERA) has conducted a 1/20 scaled model of the Ariane launch vehicle [4] to evaluate the acoustical field at take-off and pressure distributions at the bottom of the Ariane space vehicle.

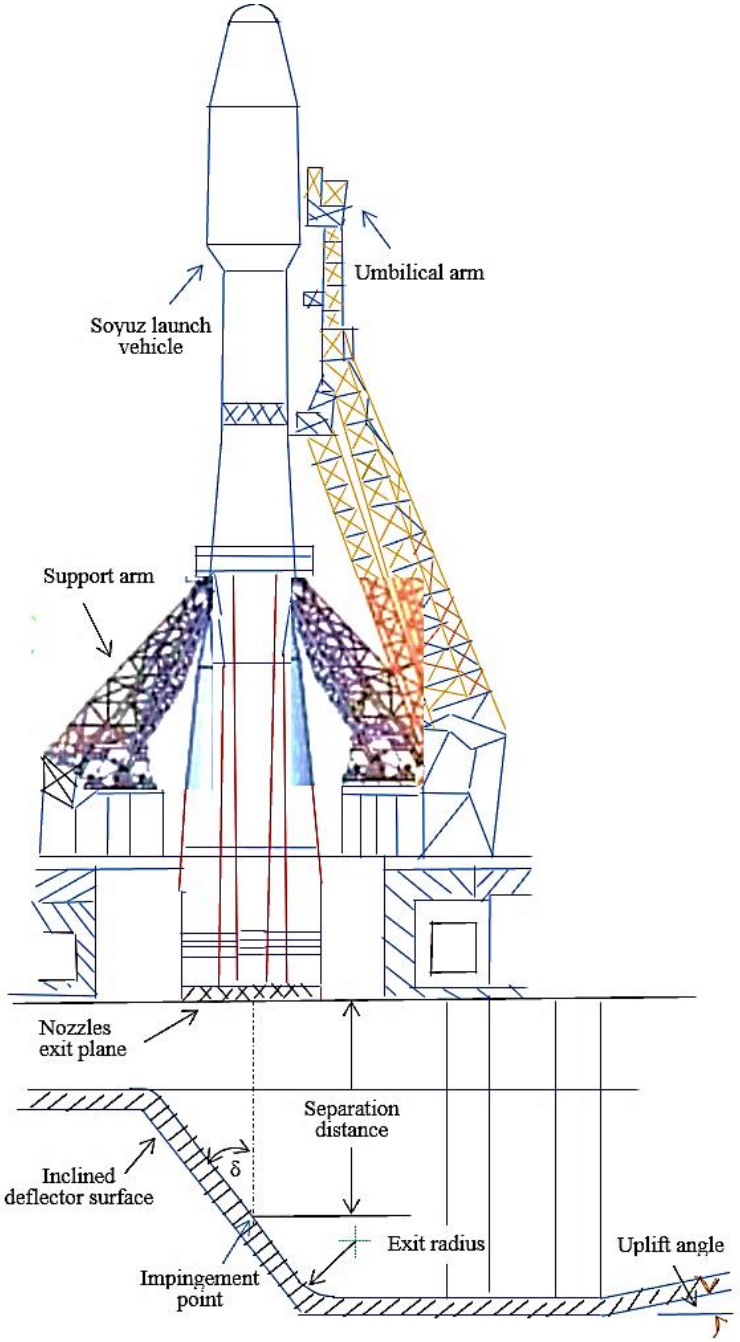

Fig. 2 Schematic sketch inclined jet deflector with Soyuz space vehicle

The jet deflection efficiency of the deflector is influenced by several geometric parameters [5] such as the jet impingement angle, the separation distance, the exit radius between the deflector surface and floor, and the uplift angle between the deflector floor and horizontal as shown in Fig. 2 with Soyuz space vehicle. The flame deflector design should be compatible with the launch vehicle and launch complex configuration or layout. The flame deflector shall be designed to minimize the exhaust impingement effects on the launch facility and to minimize the induced environmental effects on the vehicle. The nominal impingement angle minimizes the induced pressure and temperature on the vehicle and the nominal impingement angle must be a maximum of 30°. The impingement point is described as in terms of nozzle exit diameters upstream of the tangent point between flat surfaces. The separation distance and exit radius calculated based on a minimum of nozzle exit diameters.

An undesirable ARES V plume deflection might occur due to a stronger impingement angle on the deflector surface (47.5° versus 43.2°) compared by Allgood et al. [6] to an aspirator centred configuration. The plume-induced environment of a conceptual ARES V vehicle stage test at the NASA Stennis Space Centre (NASA-SSC) was modelled using CRUNCH computational fluid dynamics code. The primary

objective of their investigation was to obtain a fundamental understanding of the ARES V plume and its impingement characteristics on the B-2 flame-deflector. They noticed that the larger plume-impingement angle could result in a detached impingement shock, which would induce reversed flow upstream along the deflector surface. The pressure distribution of the flowfield was obtained by Giordan et al. [7] and their analysis reveals that the pressure is the main cause of the deflector damage.

The supersonic exhaust gas impinging model [8] has been solved by using the compressible fluid dynamics equations with the finite volume method. Daniel and Vineet [9] analysed the ARES V plume and its impingement characteristics on the B-2 flame deflector. They conclude that because the impingement angle is too large, a reversed flow formed after the exhaust gas impacted the flame deflector surface. The structural characteristics of jets flowfield deflector are analysed to predict and guide the engineering practice [10].

Donaldson and Snedeker [11] have experimentally investigated the characteristics of the free supersonic jets impinging on an inclined plate. Lamont and Hunt [12] carried out experimental investigation into the impingement of underexpanded axisymmetric jets on wedges with different apex angles (90º, 60º, and 45º) arranged symmetrically at M_e = 2.2, p_e/p_a = 1.2 and 2.0, shadowgraphs, reconstructed by means of shock polar, flow is largely inviscid.

Three-dimensional structure of an underexpanded supersonic jet impinging on an inclined plate has been numerically investigated by Tsuboi et al. [13]. The flow structure of underexpanded supersonic jet impinging on an inclined flat plate has been numerically investigated effect of plate inclination angle by Kim and Chang [14] using a total-variation-diminishing scheme with inviscid equations of fluid dynamics for M_e = 2.2, p_e/p_a = 1.2 and X_w/D_e = 3.0, T_∞ = 295ºK, on plate inclination angle θ = 45º − 90º, convergent-divergent nozzle 15º half angle. The flowfield of the rocket engine plume was obtained and the safety of the test stage was analysed. The velocity field and temperature field of the plume in the rocket engine test are obtained by Ding et al. [15]. Nakai et al. [16] have carried out experimental study of underexpanded supersonic jet emanating from convergent-divergent nozzle of 15º half cone angle impingement on an inclined plate at M_e = 2.2, p_e/p_a = 1.0 to 10.0 and X_w/D_e = 2.0 and 3.0, T_∞ = 295º K, plate inclination angle of 60º to 90º. Numerical simulations have been performed by Zhou et al. [17] have investigated the exhaust gas issuing from four liquid engine impinging on the wedge-shaped and cone-shaped deflectors. The maximum pressure and temperature in the wedge-shaped deflector are, respectively, 37.2% and 9.9% higher than those in the cone-shaped flame deflector.

Jiang et al. [18] presented an overview on progresses and perspectives of the jet impingement research for rocket launching. A comparative analysis between different jet deflectors shows that the cone-shaped deflector achieves better performance as compared to conical shaped deflector. A numerical analysis of impinging supersonic jets has been carried out for various operating conditions of rocket nozzle various operating conditions space vehicles [19, 20]. Numerical solutions of the impingement of an underexpanded axisymmetric supersonic jet on a flat plate at varied angles have been carried out by Wu et al. [21]. Computational analysis of underexpanded jets on inclined plates is carried out by Mcllory et al. [22]. Numerical simulations have been performed by Zhou et al. [23] to investigate the exhaust gas impinging on the wedge-shaped and cone-shaped deflectors. They found that the maximum pressure and temperature in the wedge-shaped deflector are, respectively, 37.2% and 9.9% higher than those in the cone-shaped flame deflector. Experiments were carried out by Brehm et al. [24] at different nozzle standoff distances from the launch pedestal simulating the lift-off of the launch vehicle. Using the reasonable shape of the flame deflector can reduce the adverse effects caused by the recirculation of rocket exhaust gas [25].

The impingement of underexpanded, axisymmetric rocket motor exhausts and cold jets on flat plates has been studied by Cobbald [26]. Main purpose of the jet deflector of a rocket launch vehicle is to deflect the jet away from the launch complex in a controlled manner to protect delicate parts of the rocket vehicle, hazards for personnel. Numerical simulations of jet impingement on a flat plate were performed by Iwamoto [27] and Matsumura, et al. [28] employing two-dimensional compressible inviscid equations. The main task of their work was to focus on numerical simulations for various inclined angles and various distances between the nozzle exit and flat plate. A multi-species unreacted flow model is numerically investigated by Hwayoung et al. [29] solving two-dimensional equations for the first-stage engine of the KSLV-II. Axisymmetric impingement of a hot jet for varying stagnation temperature range 288ºK – 1000ºK of on flat plate under equilibrium conditions are carried out by Kim et al. [30].

Numerical analysis of supersonic impingement on axisymmetric deflector at M_e = 2.2, p_e/p_a = 1.2 and 0.8 and X_w/D_e = 2 and 3 have been carried out by Prasad et al. [31]. These numerical studies reveal that the vector plots of the impinging free jets differ appreciably from the impinging vector plots numerical simulation. The numerical studies [32] of the flowfield structure in diffusers, free jets and impinging jets have been numerically investigated for a range of jet-to-freestream total pressure ratios and for different exit Mach numbers. Impingement of supersonic jets on a wedge and axisymmetric deflector [33] has been analysed using the

experimental data. Experimental pressure distribution has been used to compute boundary layer thickness, friction factor using compressible boundary layer equations for M_e = 3.1, p_e/p_a = 0.81 and X_w/D_e = 3 to 5 by Prasad et al. [34]. A three-dimensional numerical simulation has been carried out by Mehta [35] for a double-wedge jet deflector for M_e = 2.2, p_e/p_a = 0.8 and X_w/D_e = 3. The above experimental studies with cold air jets have provided a valuable insight into flow processes occurring in cold jet impingement flows. However, Numerous and experimental studies have been conducted using cold air jets instead of hot exhaust gases for analysing flow structure of the impingement jets.

An overexpanded nozzle (p_e/p_a < 1) leads to oblique shock waves at the exit of the nozzle which intersect and form diamond patterns. If the degree of overexpansion is great enough, this diamond pattern is altered to Mach disc configuration. On the other hand, a sufficiently underexpanded (p_e/p_a > 1) nozzle will lead to a similar Mach disc because of the focusing of compression waves from the jet boundary. Therefore, the structures of flowfield features depend on the degrees of overexpansion and underexpansion pressure ratio, the oblique shocks and their reflection from the Mach disc are curved, and hence termed a shock bottle. Figure 3 depicts the schematic of free supersonic jets at p_e/p_a < 1. For an underexpanded jet, the flow expands at first until its pressure balances with the ambient pressure. Then, the flow becomes overexpanded and induces compression waves, which converge to form the intercepting shocks. For an overexpanded jet, in other words, the pressure at the nozzle exit is lower than ambient pressure, oblique shocks would be generated by the compression from the ambient fluid.

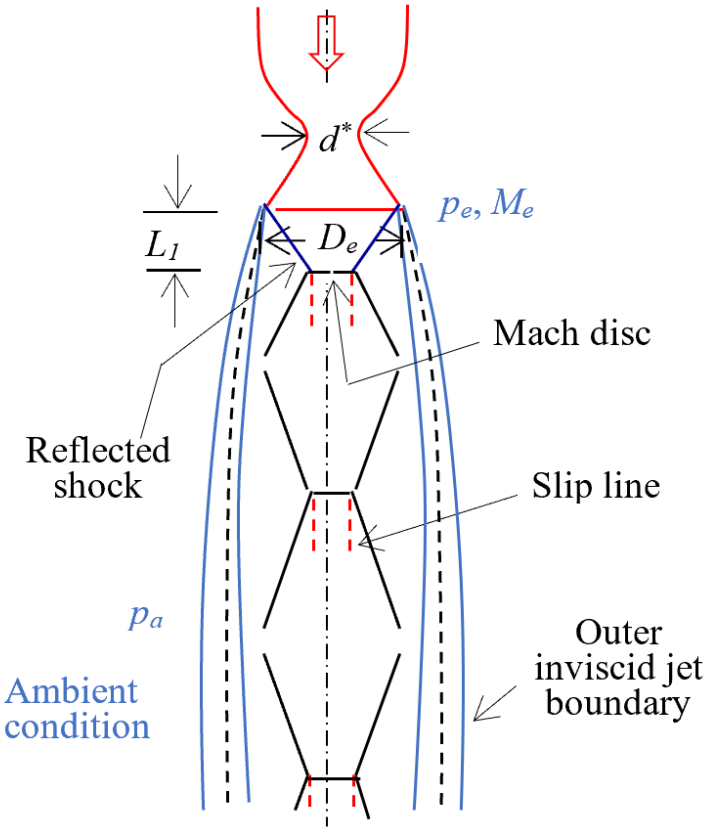

Fig. 3 Illustration of flowfield of an overexpended supersonic free jets emanating from a convergent-divergent nozzle

The impingement jet is on a double wedge deflector characterized by many discontinuities such as wedge shock wave, exhaust gas jet boundary, Mach disc, reflected shock, plate shock as delineated in a schematic sketch based [36] in Fig. 4. The impingement flowfield data are necessary for the proper design of the deflector. The exhaust gas impinges onto the launch platform and produces complex flow structures as illustrated in the schematic sketch in Fig. 4. During this stage, the exhaust gases interact with the deflector surface. Comparisons between free jets flowfield (Fig. 3) and impinging jets on a deflector (Fig. 4) show the difference of flowfield from supersonic free jets emanating from convergent nozzle on a double-wedge deflector. Due to impingement of supersonic jets produces significant flowfields characteristics in the vicinity of the deflector. The complexity of the flowfield also functions of many parameters such as M_e, p_e/p_a, and X_w/D_e.

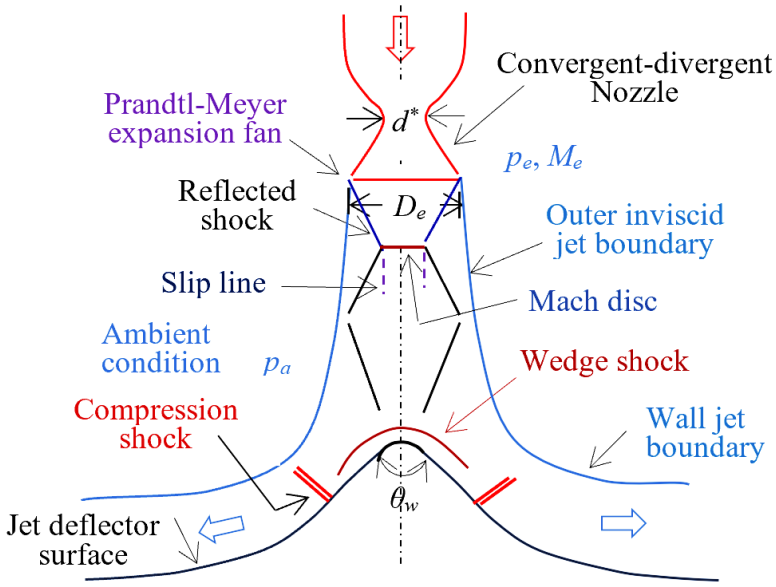

Fig. 4 Schematic sketch of double-wedge deflector along with typical satellite launch vehicle

Figure 5 shows a schematic sketch of supersonic jets impinging on an inclined plate. A plate shock is formed on the deflector and this interacts with jet shock, leading to a tail shock. The jet boundary diverts in both directions giving rise to wall jets. Such a situation arises, when the plate is placed in the first shock cell, however, when the plate is placed further downstream, the shock position, structures etc change.

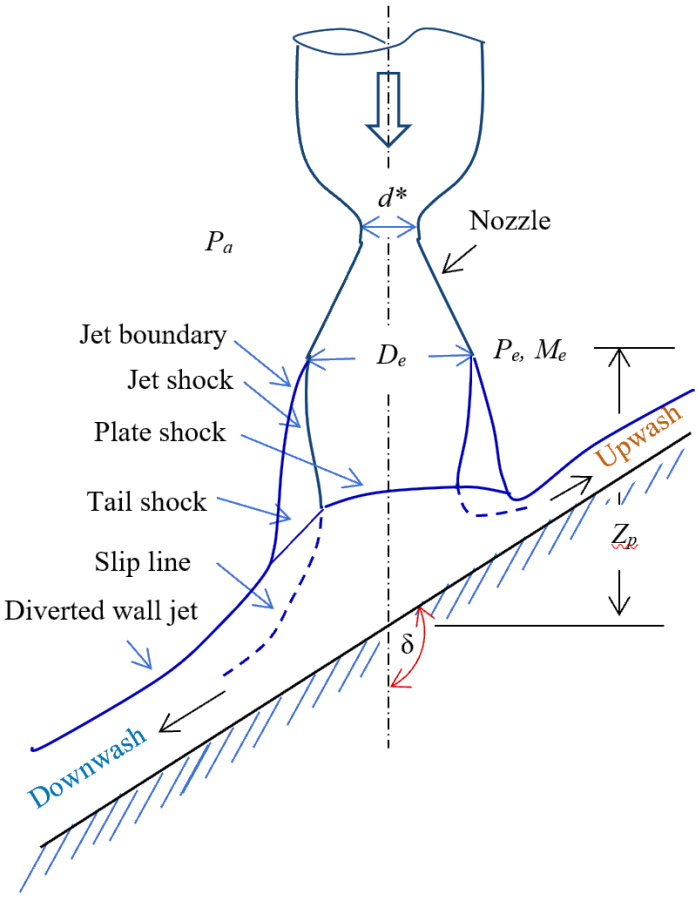

Fig. 5 Schematic sketch of flowfield of free-supersonic jets impinging over an inclined plate

The above literature survey reveals that there is considerable complexity in the fluid dynamic problem during lift-off space vehicle. Though one can tackle specific design problems through a combination of suitably tailored subscale experiments and CFD methods, there is clearly a demand for obtaining a much better understanding of the fluid dynamic aspects involved and their effects on pressure loads. The emerging field of CFD can play a significant role in this along with carefully conducted subscale tests. CFD and Machine Learning (ML) integration [37] involves using ML techniques to enhance CFD simulations, leading to faster computations, improved accuracy, and better generalization. ML is applied to accelerate expensive steps, create more robust reduced-order models for turbulent flows. ML can significantly reduce the computational time of CFD simulations by learning complex relationships from data.

The present paper employed CFD approach to simulate the impingement of the supersonic jets on a double wedge jet deflector at various operating conditions of a rocket nozzle. The numerical simulations are carried out using a three-dimensional compressible time-dependent Euler equations. The present analysis includes numerical results of hot and cold jets and their comparison with the available experimental data. The effect of ratio of specific heats is investigated on the pressure distributions over the deflector. The present study will be useful for the structure and aerodynamic design of a launch vehicle deflector. Analytical relations of oblique shock are used to analyse the flowfield of impingement from a cryogenic engine over an inclined plate.

2. Governing fluid dynamics equations

2.1 Three-dimension Euler Equations

General notation that jet impingements largely governed by the nature of the inviscid interaction that could occur if an inviscid jet having the properties of the real jet in the plan of impingement where to impinge on the surface in question [11]. The equations solved are the Euler equations describing the flow of compressible fluid. To allow the capture of shocks and the discontinuities phenomena, the three-dimensional time-dependent inviscid, compressible equations are written in conservation vector form as

$$\frac{\partial \boldsymbol{U}}{\partial t}+\frac{\partial \boldsymbol{E}}{\partial x}+\frac{\partial \boldsymbol{F}}{\partial y}+\frac{\partial \boldsymbol{G}}{\partial z}=0 \qquad (1)$$

where

$$\boldsymbol{U}=\begin{bmatrix}\rho\\ \rho u\\ \rho v\\ \rho w\\ \rho e\end{bmatrix}'\ \boldsymbol{E}=\begin{bmatrix}\rho u\\ \rho u^2+p\\ \rho uv\\ \rho uw\\ (\rho e+p)u\end{bmatrix},\boldsymbol{F}=\begin{bmatrix}\rho v\\ \rho uv\\ \rho v^2+p\\ \rho vw\\ (\rho e+p)v\end{bmatrix},\boldsymbol{G}=\begin{bmatrix}\rho w\\ \rho uw\\ \rho vw\\ \rho w^2+p\\ (\rho e+p)w\end{bmatrix}$$

are the $\boldsymbol{U}$ state vector conserved quantities with ρ, u, v, w and e denoting the density, Cartesian velocity components, and the specific total internal energy, respectively, and inviscid flux vectors, $\boldsymbol{E}$, $\boldsymbol{F}$ and $\boldsymbol{G}$ in the Cartesian coordinate. With the ideal gas assumption, the pressure and total enthalpy can be expressed as

$$e=\frac{p}{(\gamma-1)\rho}+\frac{1}{2}(u^2+v^2+w^2) \qquad (2)$$

where γ is the ratio of specific heats.

2.2 Numerical scheme

To facilitate the spatial discretization in the numerical scheme, the governing fluid dynamics Eq. (1) can be written in the integral form over a finite volume as

$$\frac{\partial}{\partial t}\int_{\Omega}\boldsymbol{U}d\Omega+\int_{\Gamma}(\boldsymbol{E}+\boldsymbol{F}+\boldsymbol{G})\vec{n}d\Gamma=0 \qquad (3)$$

where Ω is the arbitrary control volume with the closed boundary $\partial\Omega$ and control surface Γ, and outward normal facing unit vector n. The domain is divided into a finite number of hexahedral cells, and Eq. (3) is applied to each cell. The state variables $\boldsymbol{U}$ are volume-averaged values. The discretization of Eq. (3) follows discretization in space and time is done separately. The discrete values of the flow quantities are calculated at the centre of the finite volume cell having eight corners of a hexahedron. Simple vector information can be used to obtain side and surface vectors relationship along with the computational cell volume. The surface vector is independent of the choice of which partitioning surface diagonal is used to define the cell volume with eight vertices. Kordill et al. [38] method is used to compute the cell volume using of general hexahedron. A system of ordinary differential equations can be obtained by applying Eq. (3) to cells formed by six surfaces as

$$\Omega_{i,j,k} \frac{dU_{i,j,k}}{dt} + Q_{i,j,k} = 0 \quad (4)$$

where $\Omega_{i,j,k}$ is the volume of the cell, $Q_{i,j,k}$ is the convective fluxes out of the cell. The summation of the flux vectors over the six faces of the hexahedral cell is done using the average flux on each cell face.

2.3 Artificial Dissipation

In order to prevent odd-even point decoupling and oscillations in vicinity of shock waves, and to obtain rapid convergence to the steady state, artificial dissipative terms $D_{i,j,k}$ are added to Eq. (4). The artificial dissipation model considered in the present paper is based on the work [39]. A blend of forth and second differences is used to provide third-order back-ground dissipation at shock waves,

2.4 Time-stepping scheme

The above spatial discretization reduces the governing equations to semi-discrete ordinary differential equations; temporal integration is carried out using multi-stage Runge-Kutta time-stepping schemes [39]. The convergence criterion to steady-state is taken (between two successive iterations) $|\rho^{n+1} - \rho^n| \leq 10^{-4}$, where n is an iterative index. The steady-state is achieved after about 50K iterations. The numerical scheme is stable for a Courant number ≤ 2. A local time step is used to obtain a steady state solution.

2.5 Boundary conditions

Four kinds of boundary conditions are needed for the computation of flowfield, *i.e.*, deflector surface, inflow, outflow, and symmetric conditions. They are as: at the deflector wall slip boundary condition is imposed and at the out-flow boundary, the two tangential velocity components are extrapolated from the interior, while at the inflow boundary they are specified as having far field values.

2.6 Dimension of Nozzle and double-wedge deflector model

The convergent-divergent nozzles were designed for producing jet exit M_e of 2.2 and 3.1 for the exit diameter D_e as described the above. The configuration of the jet deflector is described in Fig. 6. The nozzle was having a semi-divergent cone angle of 15°. The jet deflector model consists of a cone apex angle of 70° and a tip blunt radius R_1 of $0.13D_e$. Further downstream a curvature of radius R_2 of $1.2D_e$ is provided at a location of $r = 0.7D_e$, where r is distance measured from the model axis. The deflector has a base diameter of $8D_e$. The wedge-shaped deflector is the type used on Saturn space vehicle lift-off and is configured by joining two unidirectional deflectors. This type of deflector is particularly adoptable to booster vehicles.

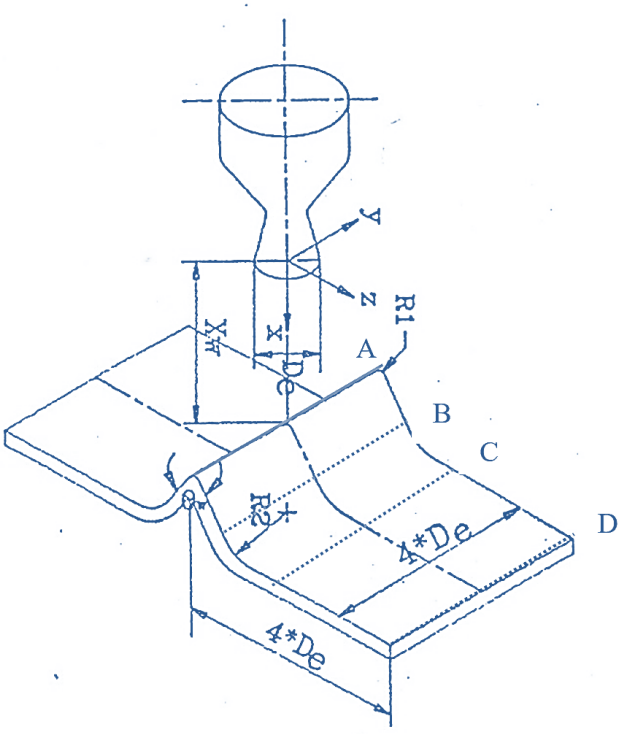

Fig. 6 Model configuration details of double-wedge deflector

2.7 Computational grid over double-wedge deflector

Supersonic jets exhausting into a normally stationary external stream are computed using inviscid flow solver developed inhouse. The initial jet radius is equal to the exit radius *i.e.* equal to $0.5D_e$. The finite element scheme is selected to generate multi-block structured method [40] to divide the computational domain in 5 zones. The grid generation was carried out in two steps. Each of these blocks is considered as a super element, which is initially described by an isoparametric finite elements [40]. The position of a plane inside an element can be described in terms of a eight edges of hexahedron cell. The computations were employed equally spaced grid points in the axial direction. Table 1 Operating parameters of nozzle and number grids used in double-wedge deflector.

Table 1 Operating nozzle conditions and number of grid points

Test case	X_w/D_e	M_e	p_e/p_a	T_e °K	nx× ny×nz
1	3	3.1	0.8	266	34×51×22
2 (Cold)	4	3.1	0.8	266	34×68×22
3	5	3.1	0.8	266	34×85×22
4	3	3.1	0.6	152	34×51×22
5	3	2.2	1.2	152	34×51×22
6 (Hot)	4	3.1	0.8	1811	34×68×22

3. EXPERIMENTAL FACILITY

All the experimental simulations of supersonic free jet and jet deflector are conducted in an Open Jet Facility (OPJ) as shown in Fig.7. High pressure dry air at 4.3×10^6 Pa at ambient temperature is fed through a 15×10^{-3} m diameter pipe line to the settling chamber and nozzle assembly. A pressure regulating valve is used to control the operating pressure. The pressure in the settling chamber is continuously recorded and monitored using a pressure gauge and a pressure transducer. The experimental set up is coupled with data acquisition. The open jet facility can be operated continuously at the maximum pressure up to about 80s.

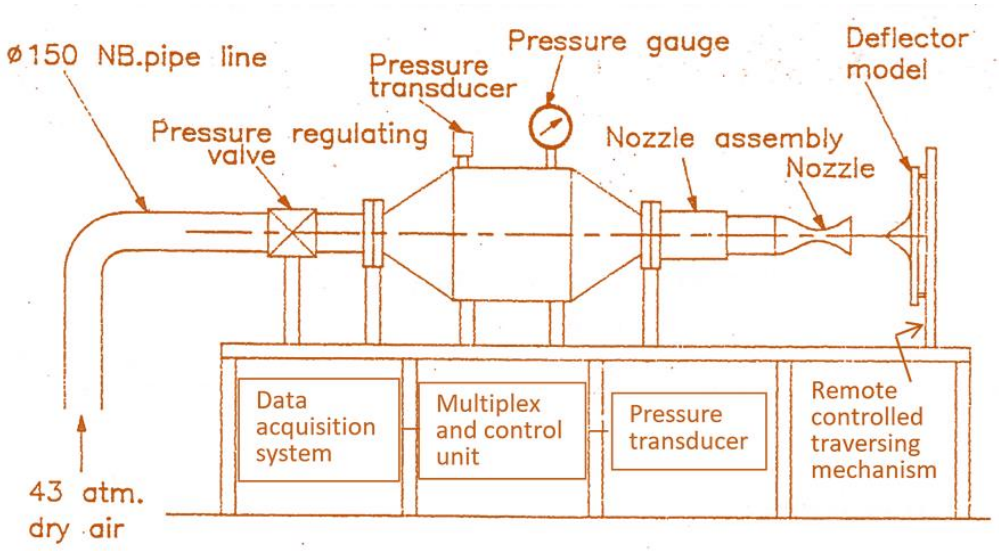

Fig. 7 Experimental set-up of OPJ

4. RESULTS AND DISCUSSION

The flowfield structures of a jet depend primarily on the operational conditions of the convergent-divergent nozzle, which are having different operating conditions as M_e, p_e/p_a, T_e and X_w/D_e. Effects of jet exit Mach number, expansion ratio and nozzle to model distance have been studied by systematically varying these parameters. Numerical simulations are carried out in the quarter plane of the double wedge deflector due to the plane of symmetry.

4.1 Impingement Flowfield over a double wedge deflector

Mach contour of impingent flowfield for M_e = 2.2 and p_e/p_a = 1.2 at different distance X_w/D_e = 2, 3, 4 and 5 are shown in Fig. 8. All the essential flowfields features are captured well. Mach contour pictures changes flowfield as a function of X_w/D_e as lift-off of space vehicle. Flow field of impinging jets on a double-wedge deflector as the space vehicle lifts off. The colour contour picture shows how flowfield alters as lift of vehicle.

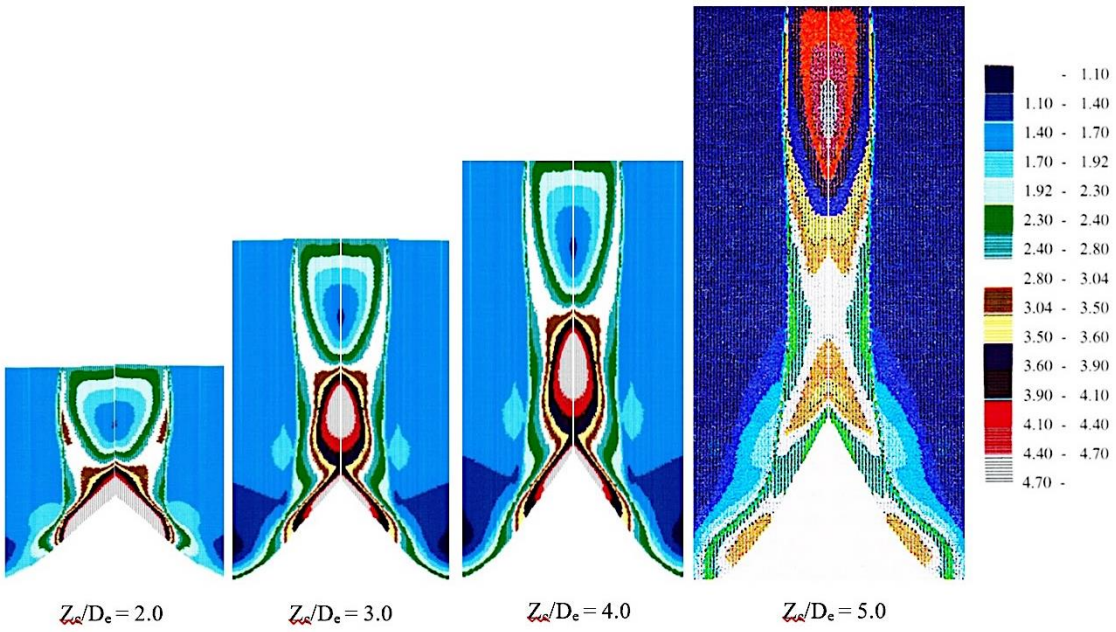

Fig. 8 Mach contour over double-wedge deflector various values of X_w/D_e

For X_w/D_e = 2, the wedge apex is downstream of the first Mach disc location is slightly displaced upstream with its downstream and its core of the jets has increased. A weak wedge shock is formed because the flow spreading the deflector has become supersonic. The flow expands due to acceleration downstream of the wedge apex and further downstream, compared due the deflector curvature is seen, and a wall jet along the deflector surface is formed. For X_w/D_e = 3, a detached wedge shock is appeared because the incoming flow has achieved supersonic speed. The wedge shock joins the jet boundary and the jet boundary gets deflected outward due to expansion at this point. A shock downstream of the apex is also noticed. X_w/D_e = 4, the wedge shock takes the shape of a Mach disc and the flowfield is identical to the flowfield as observed for X_w/D_e = 2. Further displacement of the deflector from the nozzle exit plane for X_w/D_e = 5, a wedge shock is appeared because the incoming flow achieved the supersonic speed.

As shown in Fig. 8, during the rocket launching, the flowfield of nozzle exhaust impingement behaves differently at varying lift-off heights, which is defined as the distance between the nozzle exit and the launch platform. The flowfield over the rocket changes dynamically during its lift-off stage. Thus, the flowfield over the deflector changes dynamically during its lift-off stage. When the rocket starts to lift-off, the nozzle exhaust impinges onto the launch platform and produces complex flow structures nearby. During this stage, the nozzle exhaust mainly interacts with the launch platform or the deflector system. As the rocket ascends further, the interaction between the nozzle exhaust and launch structures becomes weaker.

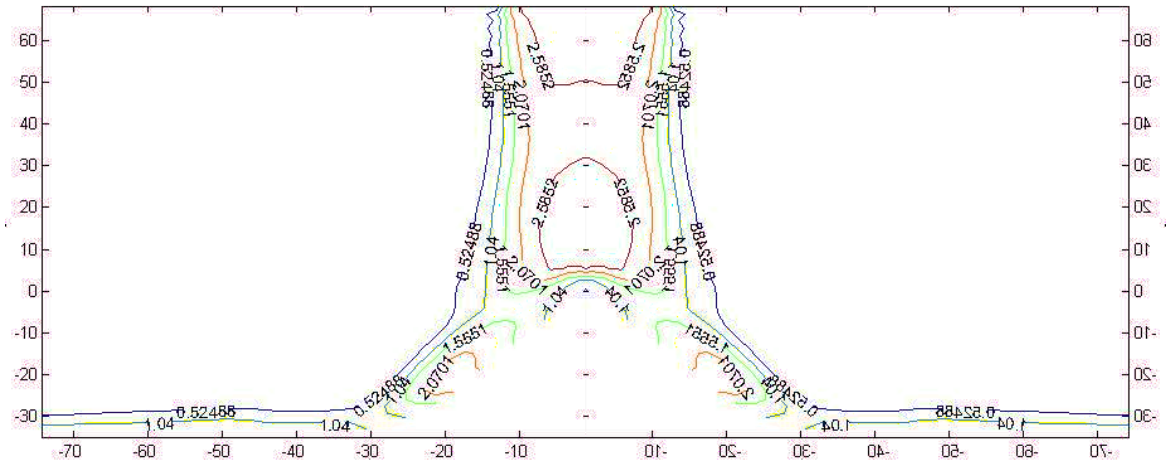

(*a*) Pressure contour

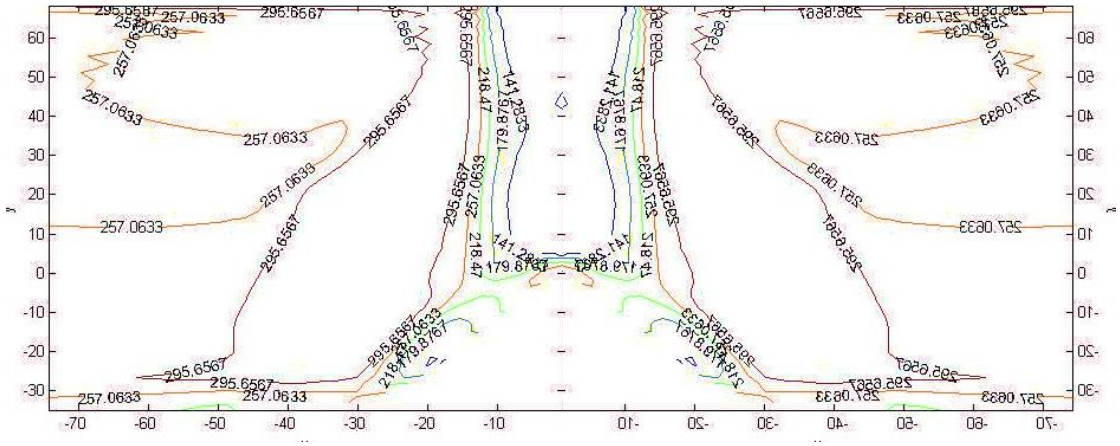

(*b*) Temperature contour

Fig. 9 Pressure and temperature contour over double-wedge deflector at M_e = 3.1, p_e/p_a = 0.8, T_e = 266ºK, and X_w/D_e = 3

For the sake of brevity, we are displaying pressure and temperature contour over a double wedge deflector in Fig. 9 for M_e = 3.1, p_e/p_a = 0.8, T_e = 266ºK, and X_w/D_e = 3. It can be observed from the figure that all the flow features are well captured by present numerical method. First Mach disc is appeared above the wedge of the deflector. It can also be noted the corresponding the pressure and the temperature values. The temperature distribution over the deflector will help to locate hot spot.

4.2 Pressure, density, Mach and temperature surface plot over double-wedge

The main purpose of this section is to displays pressure, density, Mach and temperature contour over double-wedge deflector for various operating conditions as mentioned in Table 1. Figures 10 – 13 are displaying surface plot over double-wedge deflector for different operating conditions of the nozzle such as X_w/D_e, M_e, p_e/p_a and T_e. It can be seen from the figures that the effect of operating parameters over the double-wedge deflector. Mach number over the apex of the double-wedge deflector is significant and function of X_w/D_e, M_e, T_e and p_e/p_a.

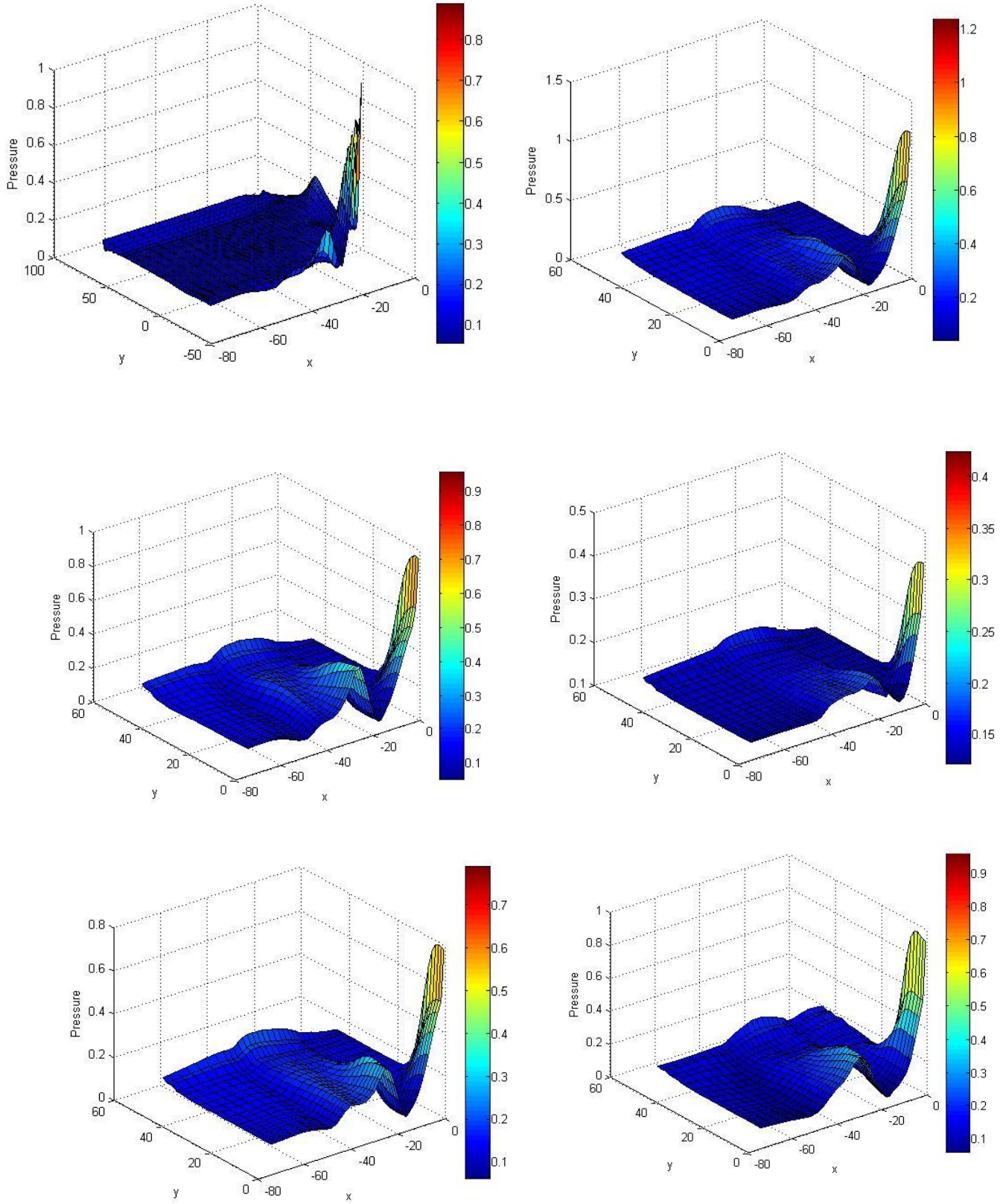

Fig. 10 Pressure surface plot over the double-wedge deflector

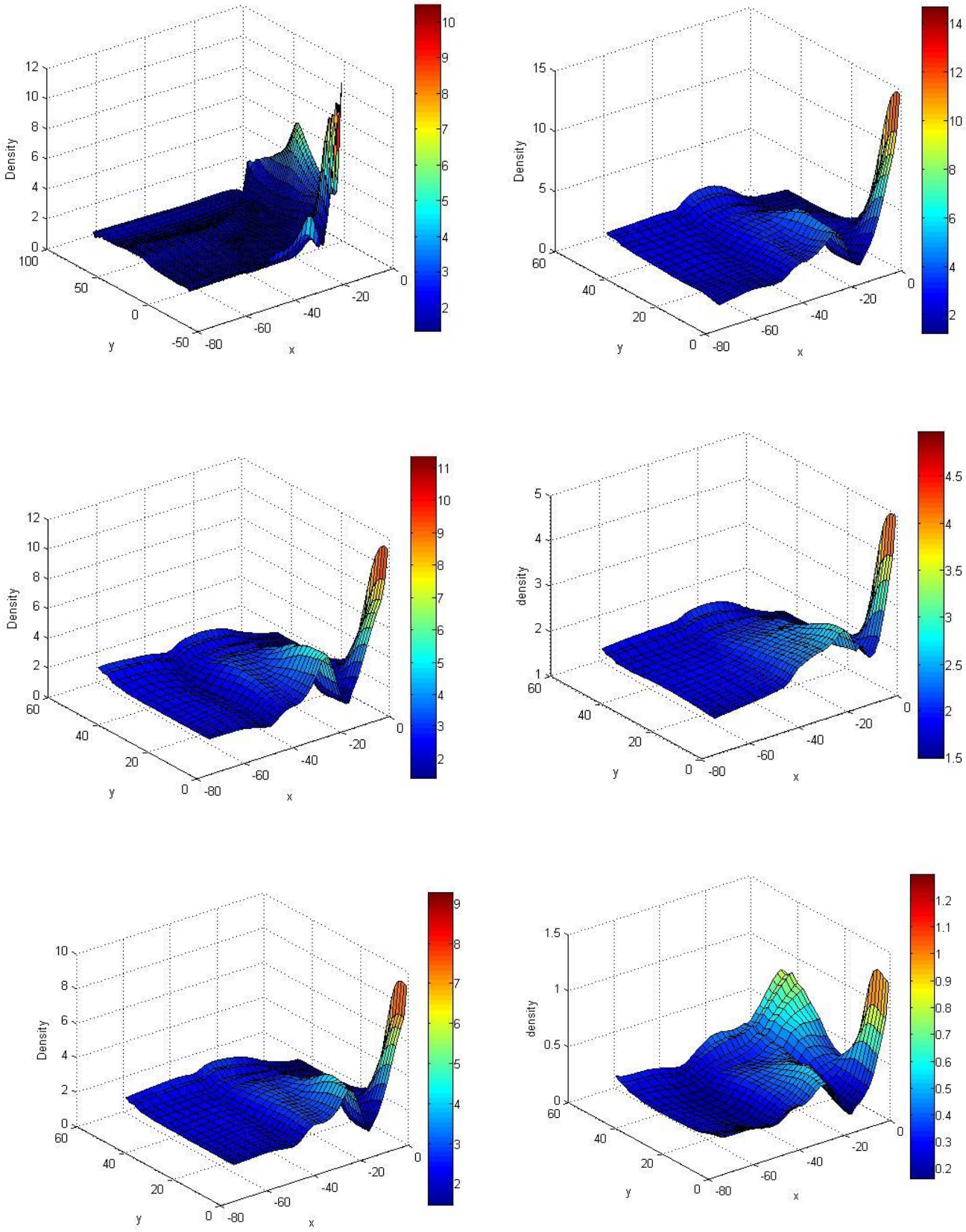

Fig. 11 Density surface plot over the double-wedge deflector

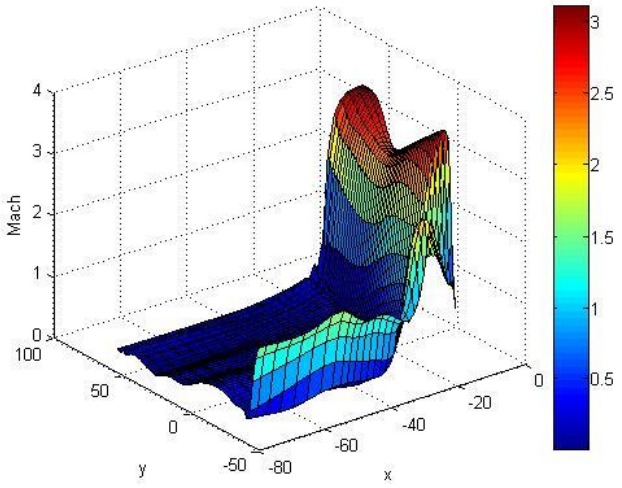

(*a*) $X_w/D_e = 3$, $M_e = 3.1$, $p_e/p_a = 0.8$, $T_e = 266^oK$

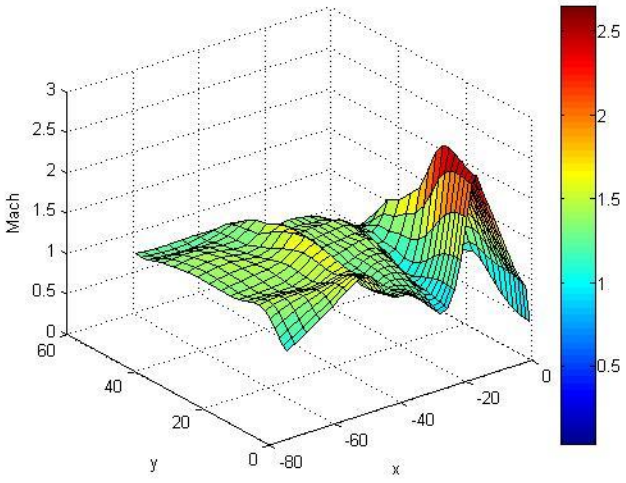

(*b*) $X_w/D_e = 4$, $M_e = 3.1$, $p_e/p_a = 0.8$, $T_e = 266^oK$

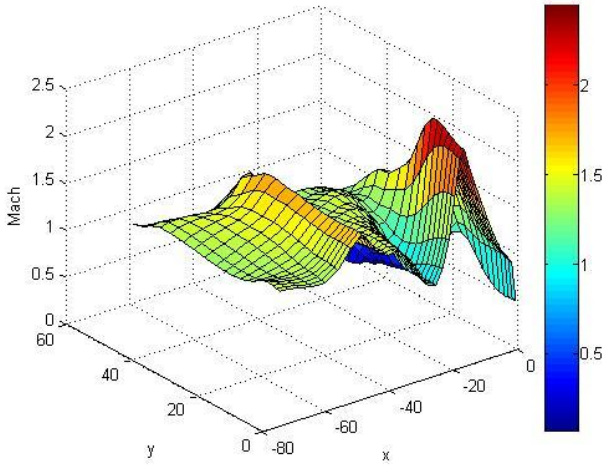

(*c*) $X_w/D_e = 5$, $M_e = 3.1$, $p_e/p_a = 0.8$, $T_e = 266^oK$

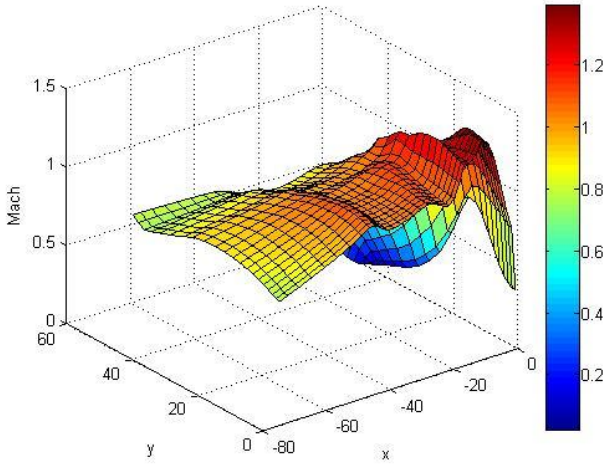

(*d*) $X_w/D_e = 3$, $M_e = 3.1$, $p_e/p_a = 0.6$, $T_e = 152^oK$

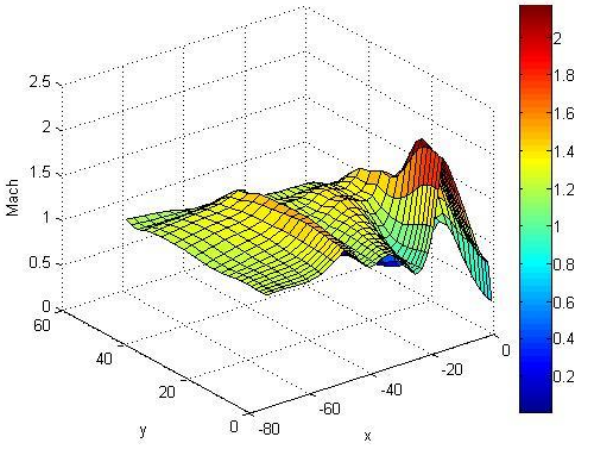

(*e*) $X_w/D_e = 3$, $M_e = 2.2$, $p_e/p_a = 1.2$, $T_e = 152^oK$

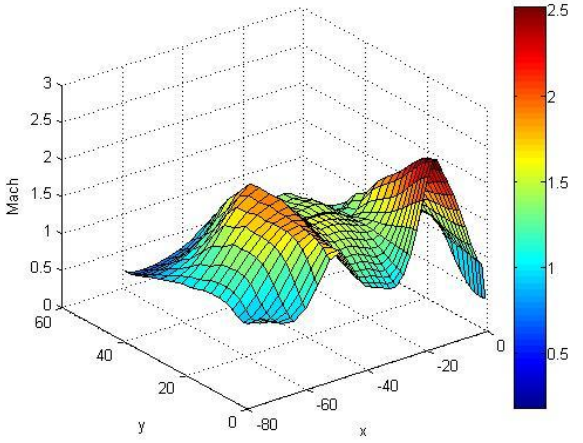

(*f*) $X_w/D_e = 4$, $M_e = 3.1$, $p_e/p_a = 0.8$, $T_e = 1811^oK$

Fig. 12 Mach surface plot over the double-wedge deflector

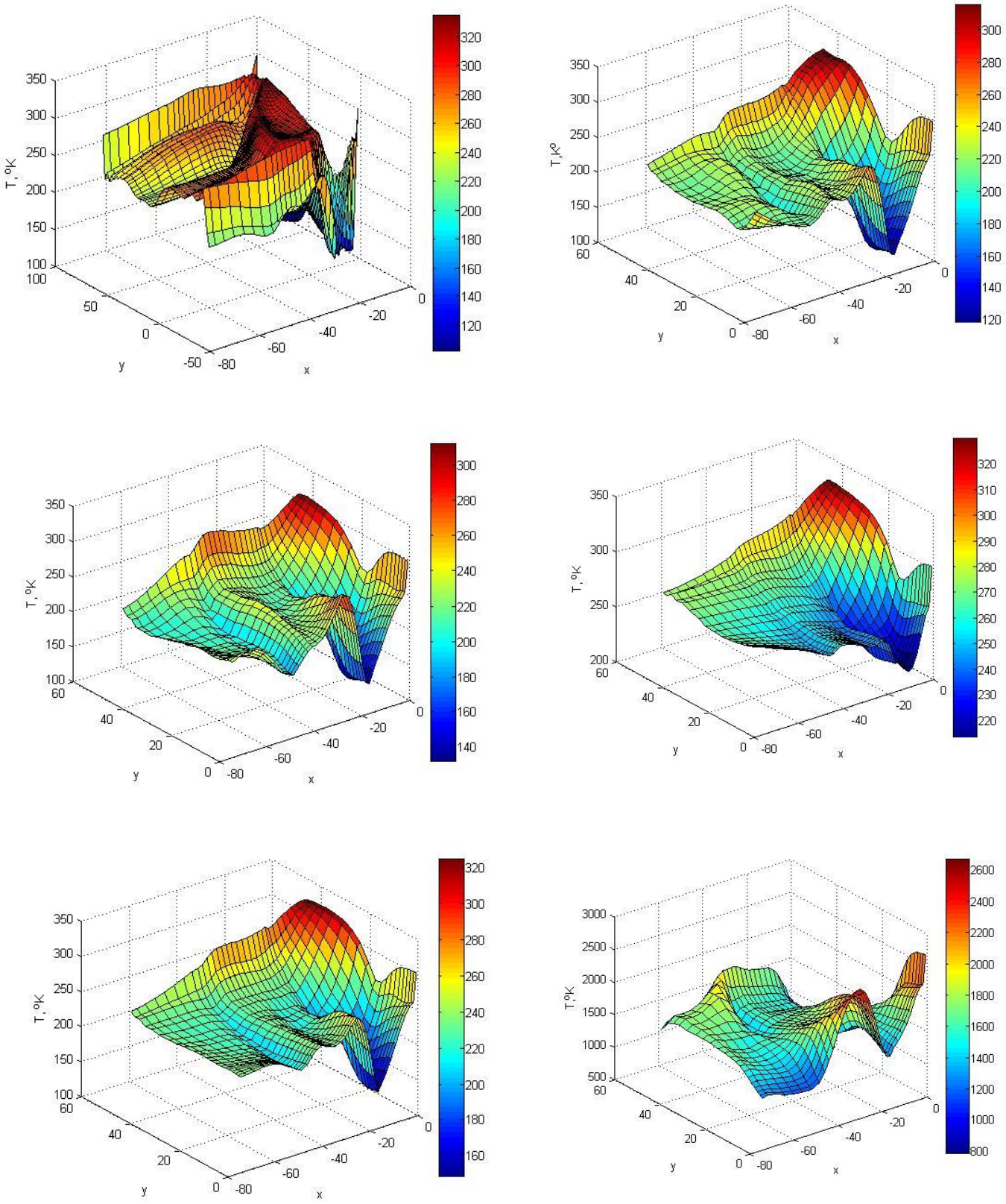

Fig. 13 Temperature surface plot over the double-wedge deflector

Figures 14 shows surface plots of pressure and temperature variations on top quarter surface of the double-wedge deflector at X_w/D_e = 3, M_e = 2.2, p_e/p_a = 1.2, T_e = 152ºK. Figure 15 shows surface plots of pressure and temperature variations on top surface of the double-wedge deflector at X_w/D_e = 3, M_e = 2.2, p_e/p_a = 1.2, T_e = 152ºK. Figure 16 displays surface plots pressure and temperature variations on top quarter surface of the double-wedge deflector X_w/D_e = 3, M_e = 2.2, p_e/p_a = 1.2, T_e = 152ºK. Please note that Figs. 14 − 16 represent surface plots on the quarter top plate of the double-wedge jet deflector as shown in Fig. 6. The computation is carried out in the quarter plane of the double wedge deflector that will save computer time as well as memory storage of the computer.

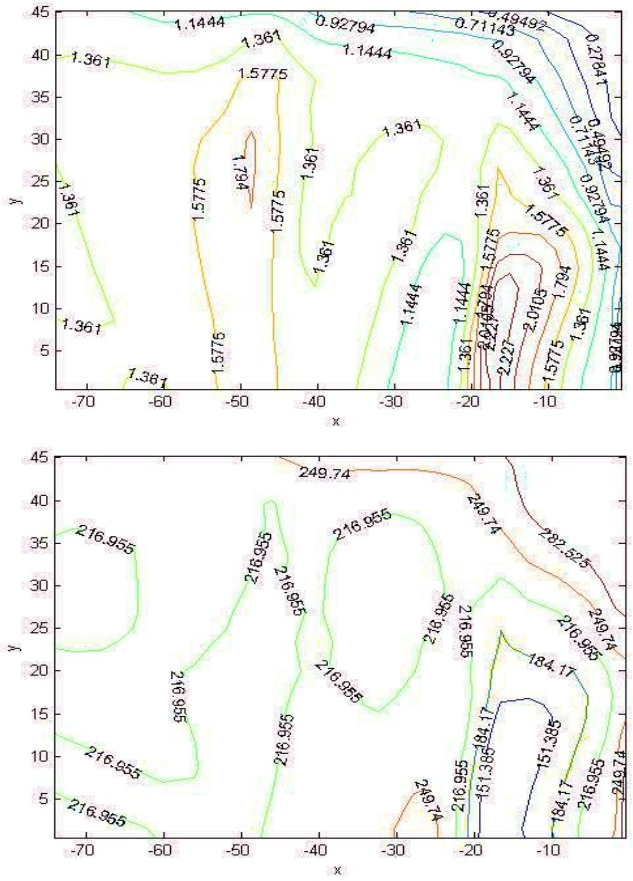

Fig. 14 Surface pressure and temperature variations on top surface of the double-wedge deflector at X_w/D_e = 3, M_e = 2.2, p_e/p_a = 1.2, T_e = 152ºK

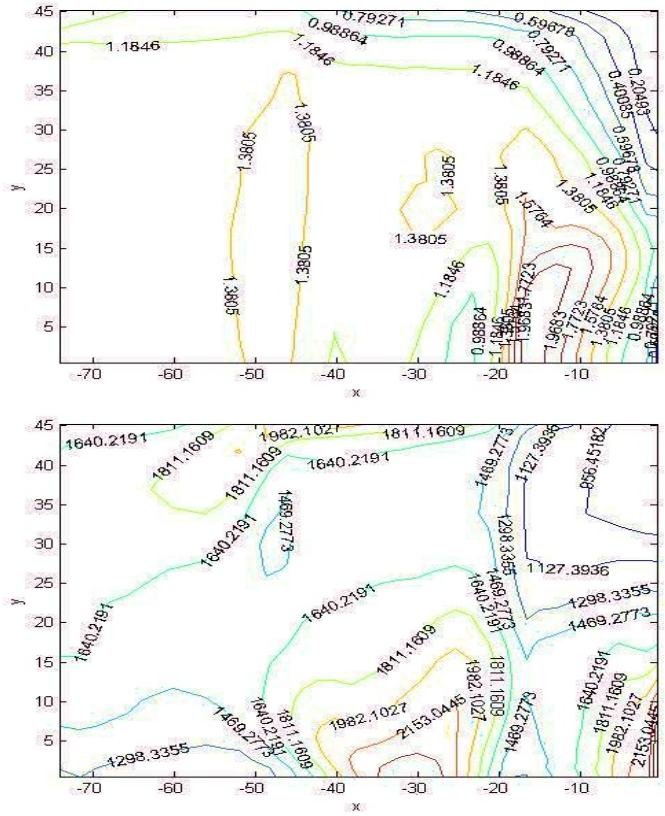

Fig. 15 Surface pressure and temperature variations on top surface of the double-wedge deflector at $X_w/D_e = 3$, $M_e = 2.2$, $p_e/p_a = 0.6$, $T_e = 152^oK$

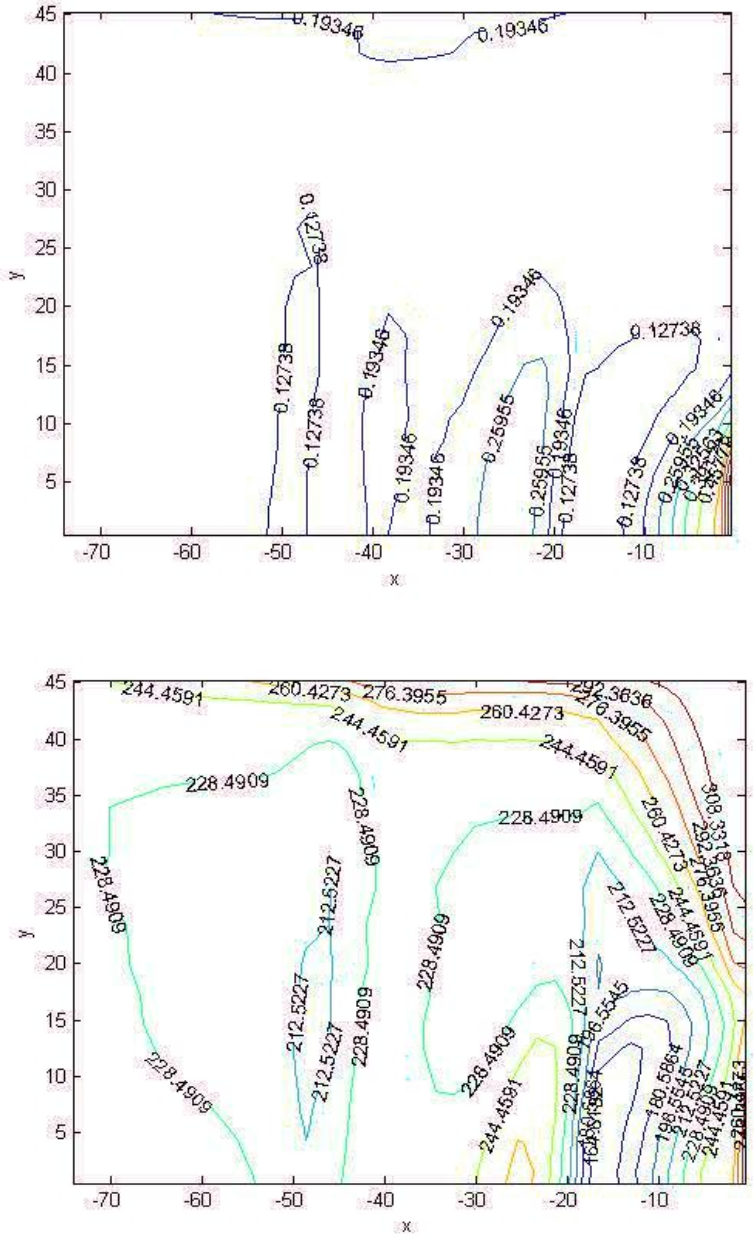

Fig. 16 Surface pressure and temperature variations on top surface of the double-wedge deflector at X_w/D_e = 3, M_e = 2.2, p_e/p_a = 1.2, T_e = 152°K

4.3 Static pressure distribution for M_e = 2.2

Figure 17 shows variations of static pressure on centre line of double-wedge deflector M_e = 2.2 and p_e/p_a = 1.2 for different values of X_w/D_e = 2, 3 and 5. At X_w/D_e = 2, pressure falls gradually from point *A* up to about X_w/D_e = 0.26, where a compression is found and further downstream, is again falls due to flow acceleration till compression initiated due to presence of the model downstream till point *C*. After the compression pressure starts to fall due to mixing of the wall jet with atmosphere. For X_w/D_e = 3, pressure decrease sharply from point *A* up to X_w/D_e = 0.1 this attributed formation of weak shock. For X_w/D_e = 5, the pressure decreases continuously along the deflector surface till compression due to deflector curvature take place. It is observed that the change in pressure variation, is confined to within a region of half nozzle diameter. From the deflector axis. In all the numerical simulations of X_w/D_e, the minimum pressure appears to occur at X_w/D_e = 0.8 and is lower than the p_a. Maximum pressure downstream of the double-wedge deflector curvature reaches almost to the same value for all X_w/D_e. The pressure distribution reveals the effect of X_w/D_e. The expansion downstream of double-wedge apex is gradually decreases up to X_w/D_e = 0.3.

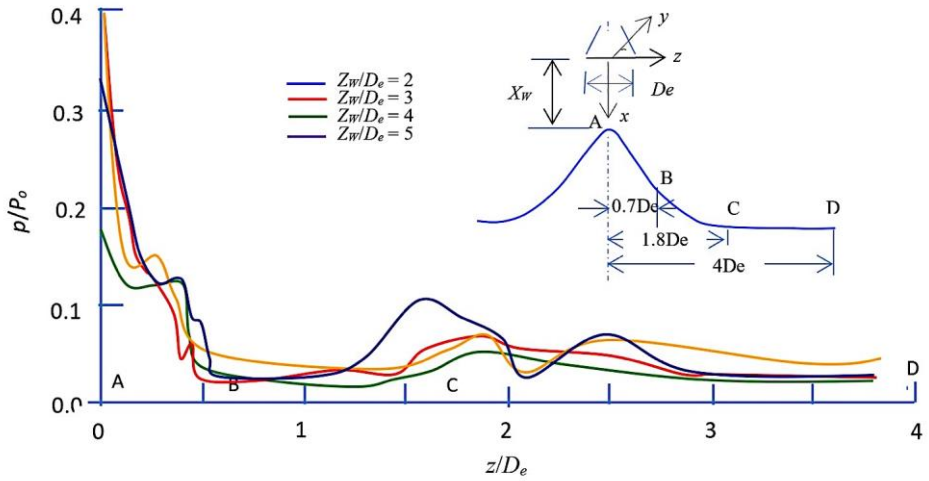

Fig. 17 Static pressure distributions along the centre-line of double-wedge deflector at various Xw/D_e for M_e = 2.2, p_e/p_a = 1.2, T_e = 266°K

4.4 Spanwise pressure distribution for double-wedge deflector

Static pressure computed on a double-wedge deflector surface along the centre-line of the deflector in the spanwise direction in Fig. 18 for M_e = 3.1, X_W/D_e = 3 and p_e/p_a = 0.8. it is observed that the pressure distributions along the deflector surface are identical at Y/D_e = 0.011, 0.22 and 0.4, except the minor pressure fluctuation on the wedge surface which may be due the three-dimension nature of the flow. These pressure variations can be integrated to determine the impingement load on the double wedge deflector.

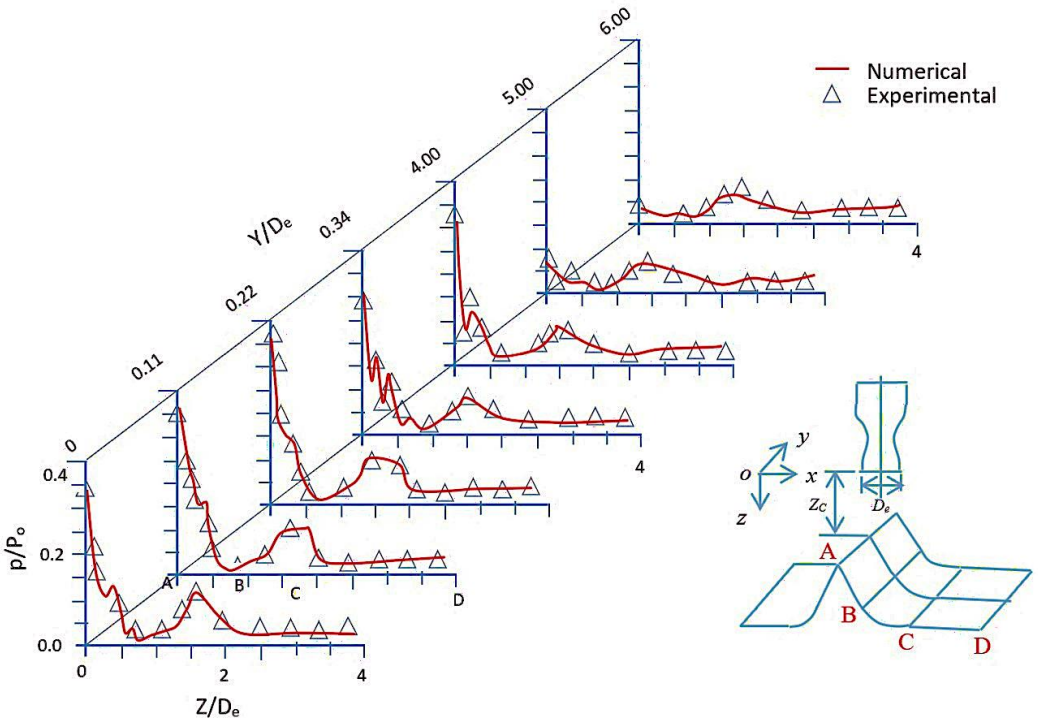

Fig. 18 Spanwise pressure distributions on double-wedge deflector surface for X_w/D_e = 3, M_e = 3.1, p_e/p_a = 0.8, T_e = 266°K

Effect of nozzle to model distance for M_e = 3.1

Figures 17 and 18 shows the pressure distributions for M_e = 3.1 at p_e/p_a = 0.8 for different X_c/D_e. This figure indicates that the behaviour of pressure distribution in similar with X_c/D_e. In all the cases continuous decrease of pressure from the stagnation point is observed till the model downstream curvature except or X_c/D_e =3. For this case compression at Z/D_e =

0.3 is observed, which is also seen in the corresponding Mach contour (Fig. 8). Compression due to model downstream curvature behaviour is similar fashion at different X_c/D_e except at $X_c/D_e = 3$. At $X_c/D_e = 3$, pressure on the model downstream curvature indicates higher increase as compared to the pressure rise at another X_c/D_e. From Fig. 8, it can be seen that the wedge shock deflected the free jet boundary appreciably. Subsequently, the jet boundary appears to turn towards the model. This deflected jet flow approaches the model downstream curvature at a higher inclination. This is likely to give stronger compression wave at the curvature. This is probably the reason for the observed higher pressure. The oscillations of the pressure distribution further downstream are possibly due to the multiple interactions of the waves with model surface and jet boundary. Such phenomena are not observed at other X_c/D_e.

4.4 Calculation of turbulent boundary layer on jet deflector surface

The viscous layer is expected to modify and influence significantly the inviscid flow field as shown in Fig. 18 the span wise pressure distributions on double-wedge deflector surface for $X_w/D_e = 3$, $M_e = 3.1$, $p_e/p_a = 0.8$, $T_e = 266^oK$. A description of the growth of turbulent boundary layer is necessary over the double wedge deflector. A simple calculation of the growth of the turbulent boundary layer by integral method of Sesman and Cresci [41] is used to compute boundary layer thickness, momentum thickness and local skin friction coefficient.

Table 2: Boundary layer parameters on double wedge deflector

x, mm	z, mm	δ, mm	δ^*, mm	C_f
7.680	23.042	0.13289	0.01859	0.00255
8.625	21.226	0.23830	0.02834	0.00246
9.601	19.202	0.52021	0.04511	0.00244
10.546	18.227	0.87995	0.07376	0.00217
12.466	15.361	0.92019	0.09540	0.00189
13.441	12.466	3.53872	0.35783	0.00134
16.306	10.546	1.60268	0.28498	0.00138
18.202	7.680	1.32161	0.17526	0.00144
23.042	4.785	1.36154	0.18592	0.00140
27.828	2.865	1.03327	0.46913	0.00146
31.668	0.044	1.05064	0.15118	0.00144
34.564	0.000	1.08325	0.15118	0.00149
41.269	0.000	0.39591	0.37338	0.00135
45.110	0.000	6.14111	0.45872	0.00137
54.711	0.000	11.17305	0.71780	0/00126
64.312	0.000	5.23585	0.37216	0.00147
73.914	0.000	5.35259	0.41148	0.00140
83.515	0.000	5.79942	0.45944	0.00135
93.116	0.000	6.06643	0.49255	0.00131

Table 2 displays boundary layer thickness δ, momentum thickness δ^* and skin friction coefficient C_f. It can be observed from this table that the separation of the boundary layer is not noticed. However, the comparison of boundary layer with the experimental results shown good agreement [42].

4.5 Impingement load on the double-wedge deflector

Integration has been made using trapezoidal rule for one case of the wedge model where complete surface pressure distribution is available as shown in Figs. 17 and 18.

$$C_W = \frac{L}{T} \tag{5}$$

$$L = \int_{y=-\frac{b}{2}}^{\frac{b}{2}} \int_{Z=-\frac{l}{2}}^{\frac{l}{2}} (p - p_a)\sin\varphi \, dsdy \tag{6}$$

$$T = p_e A_e \left\{ \gamma M_e^2 \left[\frac{(1+\cos\theta_N)}{2} \right] + \left(1 - \frac{p_a}{p_e}\right) \right\} \tag{7}$$

For wedge deflector model the value of load coefficient is obtained by making use of the pressure distribution (Figs. 17 and 18). This gives the value of $C_W = 0.82$ for the $M_e = 3.1$ at $p_e/p_a = 0.85$ and $X_c/D_e = 3$. This is comparison with the corresponding case of axisymmetric deflector [34], indicate that the load coefficient for wedge model is higher (approximately = 45%).

4.6 Impingement of hot jet on wedge deflector

On test was conducted with a jet of higher total temperature than the cold jet test using a rocket motor

[43]. The exhaust from the rocket motor chamber pressure and static pressure distribution on a wedge deflector model is shown in Fig. 19. During this test, time histories of rocket motor chamber pressure and static pressure distribution on the deflector surface are measured. The test conditions are $M_e = 3.1$, $p_e/p_a = 0.85$, $T_o = 3000^oK$ and ratio of specific heats of 1.24. Fig. 20 shows the time history of rocket motor chamber pressure which indicates a sharp increase to peak value within 0.045s and subsequent gradual decrease to almost a constant value of 5.7 MPa. After about 6s, pressure decreases to ambient value to burn out of the rocket motor. Surface pressure at seven locations on the deflector model are also recorded in real time. A typical surface pressure time history is shown in Fig. 20. The time history of this pressure almost follows the trend of pressure time history of the rocket motor chamber. It is observed that the pressure is almost constant during the period 0.5 to 1.5s after the start of the test. Afterwards, the pressure starts to decrease due to the reason that the erosion of the basic deflector surface, is higher compared to the graphite block in which the pressure port is located. At this time, graphite block is likely to protrude above the basic deflector surface, giving rise to a possible flow separation. Hence the correct surface static pressure is not sensed by this pressure port provided in the graphite block. Hence the pressure signal between 0.5 to 1.5s has been assumed to be the correct static pressure on the model surface for all the seven channels.

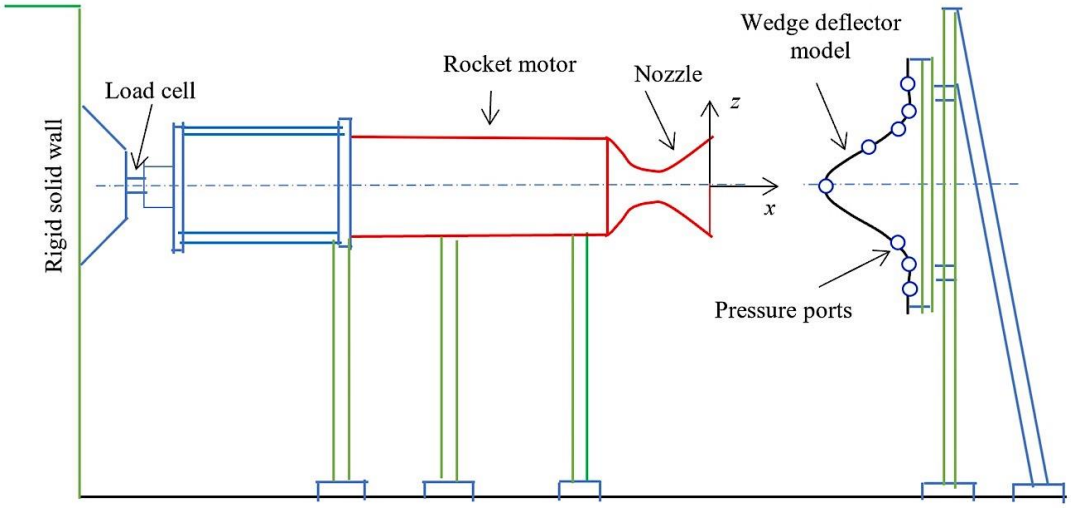

Fig. 19 Schematic of diagram for hot jet impingement experimental setup

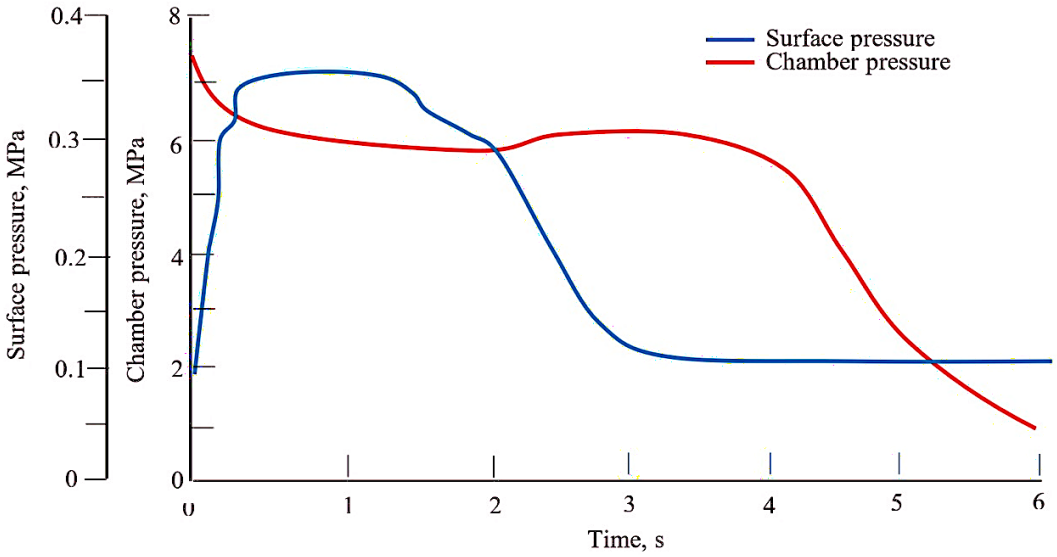

Fig. 20 Time history of rocket motor chamber pressure and typical static pressure on double-wedge deflector

4.7 Comparison of hot and cold jet results

Static pressure distribution obtained on the deflector model at hot jet condition is compared with the data obtained from the cold jet test. This shows the effect of jet temperature T_o and ratio of specific heats γ. It is usual practice to nondimensionalise the static pressure on the surface with chamber pressure P_o. Comparison of these two-pressure distribution is shown in Fig. 20. Values of P_o for hot and cold jets are different due to different value of γ for the same p_e/p_a and M_e at the nozzle exit. Hence the value of p/P_o differ downstream of the curvature R_2, although the ambient pressure for both the cases is identical. Therefore, the cold jet pressure distribution normalised with P_o cannot be used for predicting the pressure distribution for the hot jet case.

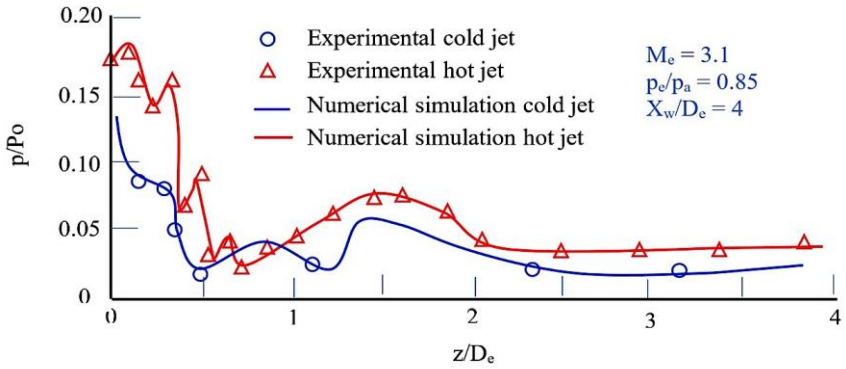

Fig. 21 Comparison between numerical and experimental static pressure distributions with hot and cold jets on a double-wedge deflector surface

In order to able to compare these two pressures and to avoid the above difficulty, as well as to incorporate the effect of specific heat ratio γ, the results are presented in the form of pressure coefficient Cp which is defined as

$$C_p = \frac{(p-p_a)}{0.5 p_e \gamma M_e^2} \qquad (7)$$

For computing Cp, the values of γ used for the cold jet and hot jet cases are 1.4 and 1.24, respectively. The value of M_e and p_e/p_a are 3.1 and 0.85 respectively, and they are same for both the cases. Comparison of Cp distribution obtained for hot jet test with the cold flow test is shown in Fig. 22. This indicates that the comparison is good in the downstream portion, whereas differences exist in the stagnation zone. This difference may be due to the higher temperature of the hot jet, which may be giving rise to a flowfield around the stagnation zone differs from the cold jet cases. It is observed that the values of stagnation zone pressure obtained in the hot jet case is lower (approximately 25%) than the present obtained in the cold case. This indicates that the results obtained from the cold jet tests can be used for a conservative design of an actual jet deflector.

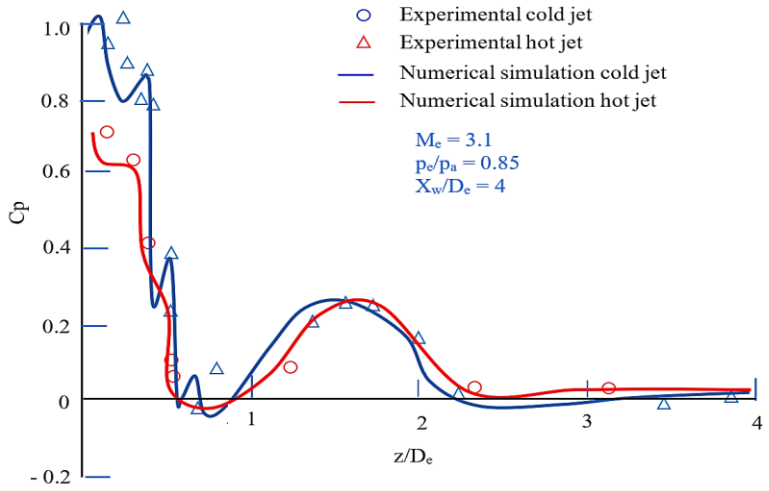

Fig. 22 Comparison between numerical and experimental pressure coefficient distributions with hot and cold jets on a double-wedge deflector surface

Figures 21 and 22 show a comparison of pressure distributions for the rocket and air jets impinging on deflector. For deflector the agreement is quite close, but in all cases the rocket jet impingement process somewhat lower. The pressure produced by the rocket jet are lower than those produced by the cold jet. The main conclusion of this study is therefore that the differences between rocket exhaust and cold gases do not significantly affect impingement pressure found at the deflector of a flat plate.

Figure 23 shows the pictures of the deflector surface after the hot jet test. The pattern seen on the surface shows the erosion on the surface. During the hot test, the deflector surface material melts and flows along the surface, similar to oil flow pattern obtained during the cold flow test. Therefore, comparison of the erosion pattern on the deflector surface after the hot jet test with the oil flow pattern obtained during the cold jet test, should indicate similarity. Oil streak pattern on the model surface is obtained using oil flow technique at the same p_e/p_a and X_c/D_e, using cold air jet.

Comparison of these this picture indicates that there is similarity between the pattern observed in both cases. This indicate that oil flow pattern on the model surface observed in cold jet test can be made use of the approximate identification of the regions where erosion is likely to be more in the hot jet condition, this information may be useful for adopting some methods to minimize the erosion in that region.

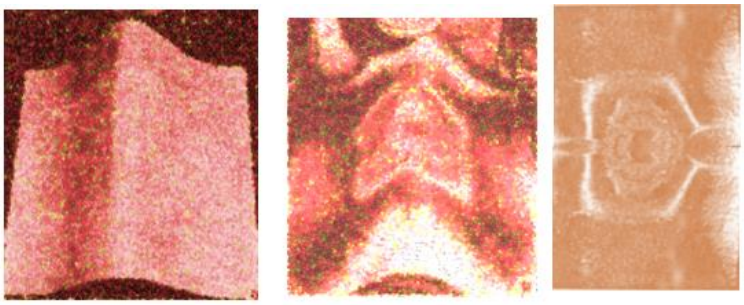

Fig. 23 Comparison between numerical and experimental surface pressure profiles on a double-wedge deflector surface with hot and cold jet

We are here comparing numerical results of cold and hot test cases number 3 and 6 as shown in Table 1. Figure 24 shows pressure, density, Mach contour and temperature contours of cold and hot tests, respectively. The comparison shows significant difference in temperature contour between cold and hot text cases numerical results. The main conclusion of this study is therefore that the differences between rocket exhaust and cold gases do significantly affect impingement pressure and temperature on the deflector surface. It is important to mention here that these numerical results also reveal the effect of ratio of specific heats on contour. These also appeared in Figs. 21 and 22.

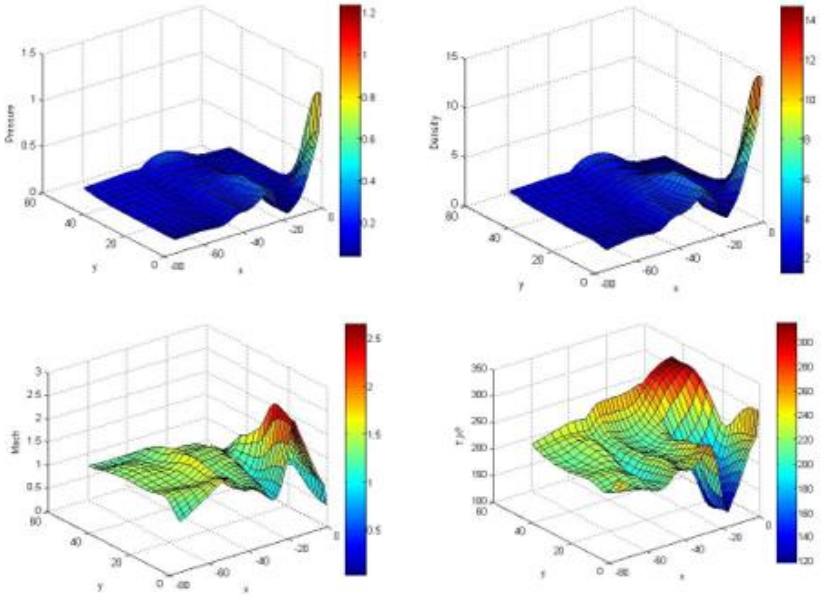

(*a*) $X_c/D_e = 4$, $M_e = 3.1$, $p_e/p_a = 0.8$, $T_e = 266°K$

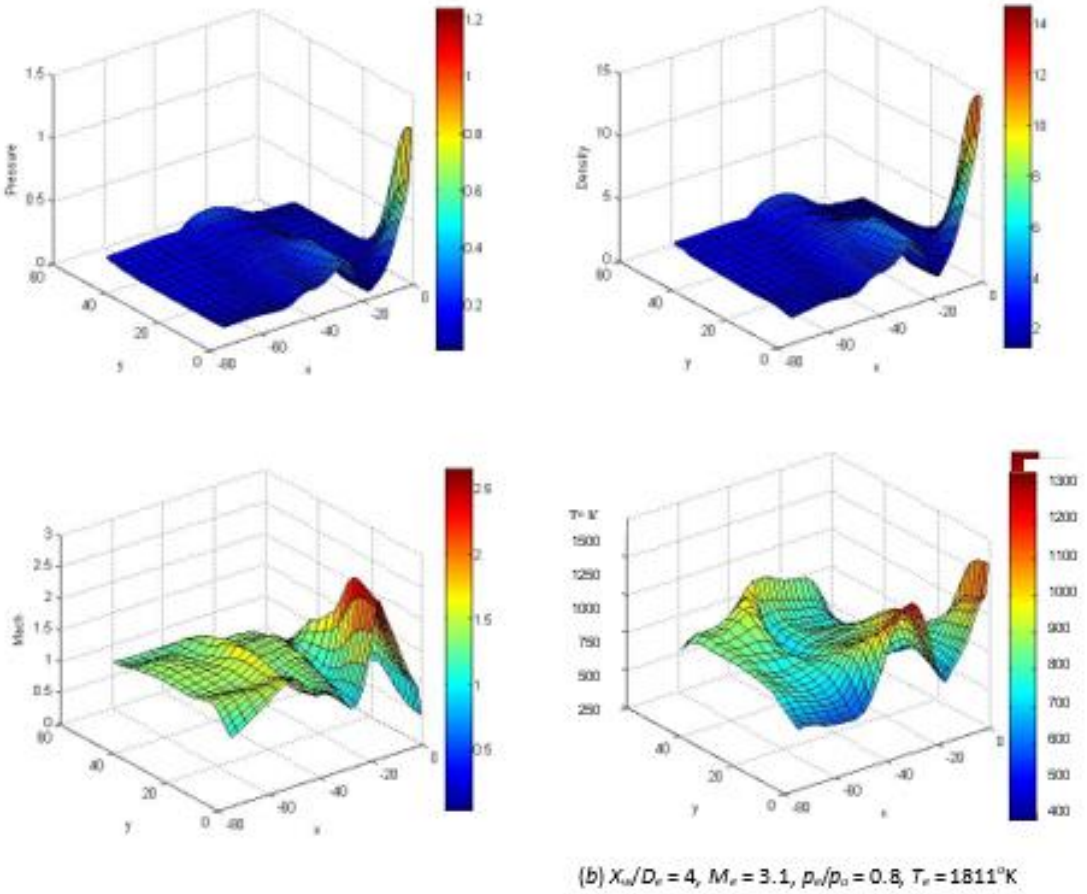

Fig. 24 Pressure, density, Mach and temperature contour over the double-wedge deflector

4.7 Numerical simulation of Impingement jet on a typical deflector

This problem is solved when the L-40 engine is operated during the lift-off time. The boundary conditions are enforced by using the idea of image cells on the plane of symmetry as shown in Fig. 25. On the nozzle exit plane of L-40 engine, the following conditions are taken for the computational purposes: ρ = 0.081 kg/m^3, T = 1144.907 K, M = 20.927 kg/mol, Cp = 1978.581 J/kg K, M_e = 3.689. At the nozzle diaphragm of the core motor and solid wall of the jet deflector no normal flow conditions are applied. For quiescent external condition, the ambient pressure is imposed on the remaining sides of the computational domain.

The boundary conditions are enforced by using the idea of mirror cells at the centre of axisymmetric free jet. At the nozzle exit, all of the flow properties are prescribed since the incoming flow is supersonic. On the deflector surface, the flow properties in the image cell are taken as those of the adjacent boundary cell, except that the normal component of the velocity is reflected to ensure the impermeability condition. For quiescent external condition, the ambient pressure is imposed as the outer boundary condition which is considered about 8 times the nozzle exit diameter.

A simple algebraic grid generation program [40] is used to generate the mesh. Fig. 25 shows the grid system for the half of the symmetric plane of the flowfield where *FG* represents the jet coming out from the nozzle, *GH* is solid motor diaphragm, *HA* is the line of symmetry, *ABCD* is the deflector surface, and *DE* and *EF* are free boundaries. The computational is discretized with hexahedral cell of non-uniform mesh spacing. The numerical computations are carried out on 48×141×91 grid points which are selected after grid independency check.

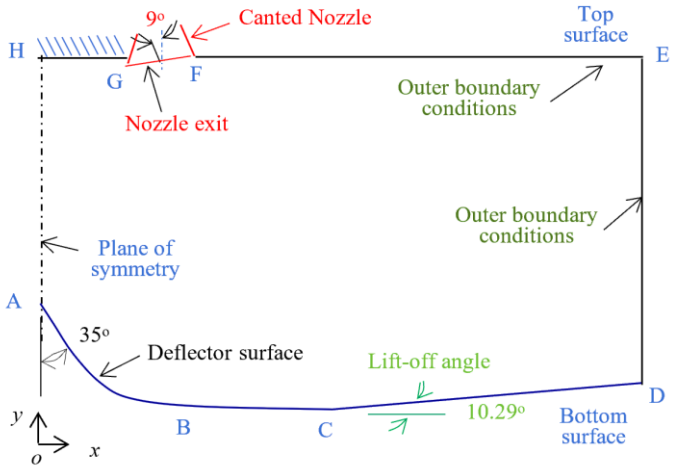

Fig. 25 Computational domain with top and bottom surfaces

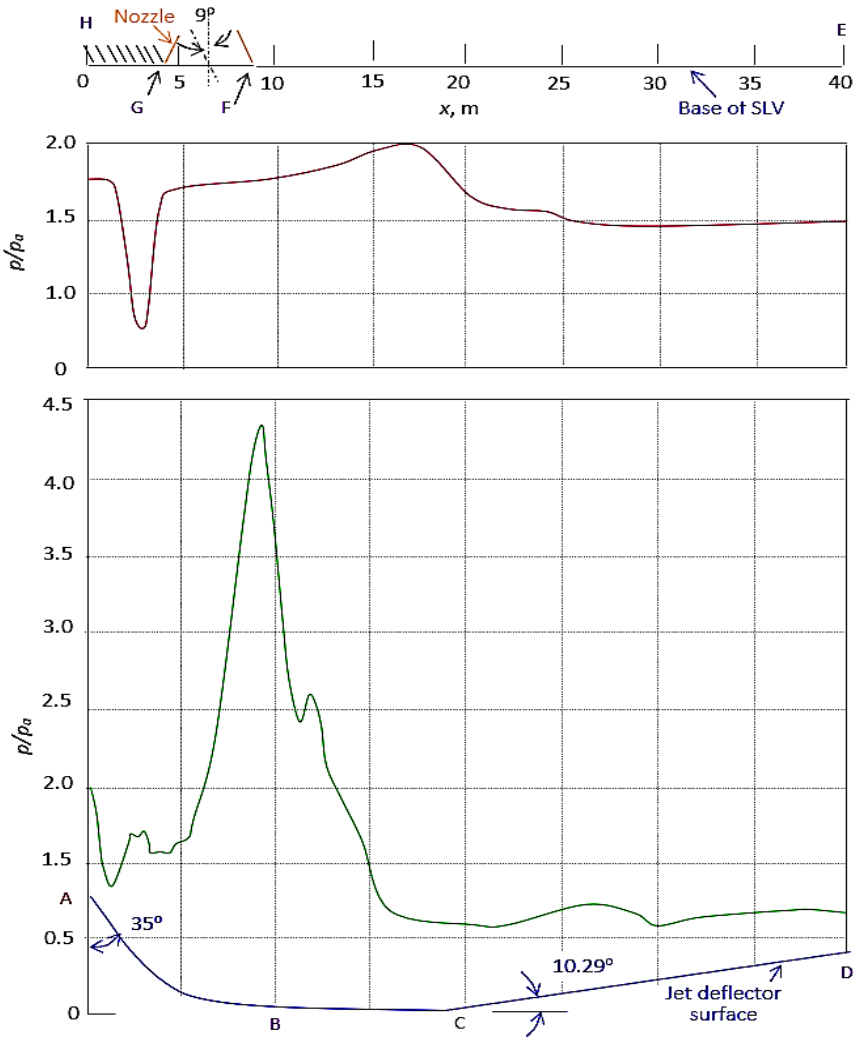

Fig. 26 Pressure distributions over top and bottom surfaces of the deflector

Static pressure distribution along the deflector surface has been shown in Fig. 26. A higher pressure is observed at a location downstream of the apex of the deflector which is impingement region of the jets. Figure 26 shows pressure on the base of the launch vehicle. It can be seen from the pressure distribution that the

diaphragm is having pressure below the ambient pressure.

4.8 Analytical analysis of inclined plate jet deflector

An oblique shock wave occurred when the supersonic jet impinges on a inclined plane. Using the gas dynamics equations and system geometry, the following equation is derived

$$\frac{1}{M_e^2} = sin^2\beta - \frac{(\gamma+1)}{2}\frac{sin\beta sin\delta}{cos(\beta-\delta)} \quad (8)$$

where M_e is nozzle exit Mach number, β is angle between flow direction and shock wave, δ is angle between flow direction and impingement surface, and γ is ratio of specific heats. Figure 27 shows the nomenclature of the impingement of oblique shock strike on an inclined plate,

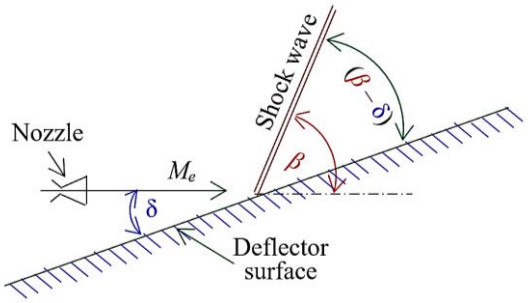

Fig. 27 Supersonic jet impingement of an inclined plate

Based on the above equation, the plot of $(\beta - \delta)$ versus δ is presented in Fig. 28. It is observed that at $\delta >$ 50°, the curve becomes asymptotic with the ordinate implying that the direction of the shock wave tends to deviate the most from that of the deflected plane. Since such a condition would result in the interference of the shock wave with the upstream jets, a deflection angle of 50° is considered the *critical value*. It is worth to mention here that the critical angle is not important when the exhaust impinges on the apex of a cone or double-wedge shaped deflector. It is also seen that at 20°, $(\beta - \delta)$ reached a minimum value, implying that the shock wave direction is in vicinity with the deflected jet direction. Since such a condition is to the most desired one, therefore, $\delta = 20°$ is considered the *ideal* value. The ideal deflection angle demands increased depth of the deflector and hence a compromise is to be struck between the ideal deflection angle and the critical deflection angle. Therefore, a deflection angle of 30° is treated as the optimum deflection angle. The impingement angle is also important to the determination of the forces acting on a deflector in the impingement area.

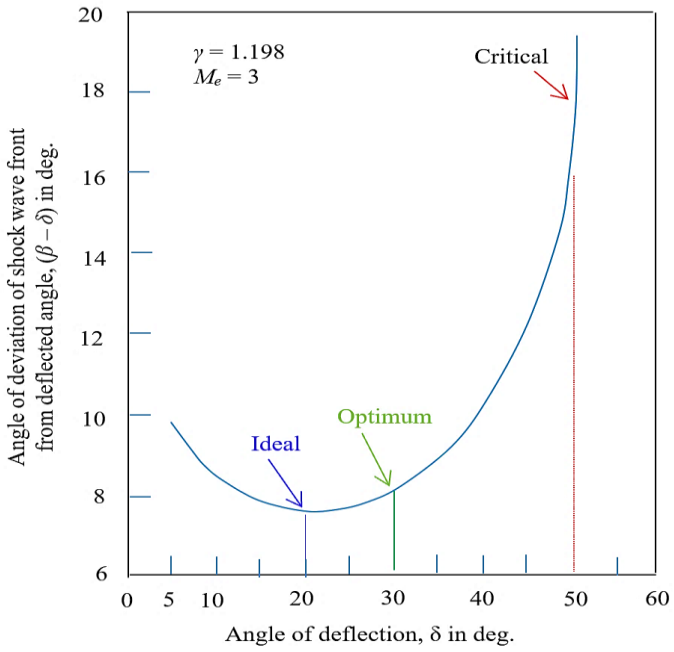

Fig. 28 Effect of deflection angle δ on shock wave propagation $(\beta - \delta)$

The axial velocity of the jet stream on the jet axis can be determined by the following empirical formulas: [44]. The axial velocity from the nozzle exit within which the plume velocity equals that at the nozzle exit is given by

$$x = \frac{D_e}{0.106} \tag{9}$$

when the distance x is greater than the value by this equation, the plume velocity on the axis decreases according to the following relation:

$$log_{10}\left(\frac{V_x}{V_e}\frac{x}{D_e}\right) = 0.79 - 33\left(\frac{r}{x}\right)^2 \tag{10}$$

where V_x is axial velocity at gas on jet axis at x. V_e is axial velocity at nozzle exit, and r is radius at gas jet parameter from axis into ambient air

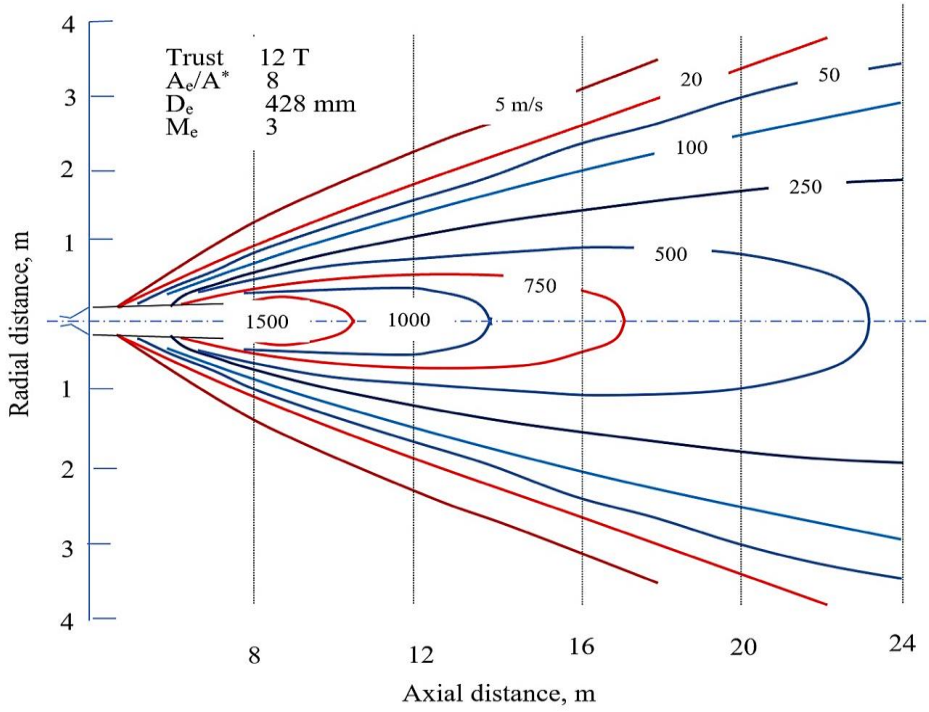

Fig. 29 Velocity distribution of plume for cryogenic liquid engine

An oblique shock wave is a flow discontinuity which is occurred when a supersonic jet stream impinges on a surface. Supersonic with Mach number M_e impinges on a deflector inclined at an angle δ to the stream flow direction. Figure 29 shows typical velocity distribution patterns in free-flowing rocket engine exhaust at sea level for cryogenic engine operated at 12 N thrust. The distance between the nozzle exit and to the jet deflector surface is square root of thrust.

CONCLUSIONS

Numerical analysis of cold air emanating from convergent-divergent nozzles have been carried out for different operating parameters of rocket nozzle. Experimental investigations of supersonic jets of cold and hot air emanating from conical nozzles have been conducted. Effect of ratio of specific heats on the flowfield and pressure profiles is studied and compared with available data. Pressure profile on the base of vehicle shows recirculation zone. Impingement jet load on the deflector surface is calculated by integrating surface pressure over deflector. Analytical relations are used to obtain jet profile. Effect of deflection angle on shock wave propagation shows the ideal. Optimum and critical condition for deflector.

Nomenclature

A_e	nozzle exit cross-sectional area
A^*	nozzle throat area
D_e	nozzle exit diameter
d^*	Nozzle throat diameter
e	specific total internal energy
$\boldsymbol{E}, \boldsymbol{F}, \boldsymbol{G}$	inviscid flux vector
M_e	exit nozzle design Mach number
P_o	stagnation pressure
p	pressure
p_e	pressure at the nozzle exit
p_a	ambient static pressure
L_1	first shock cell length
T_e	temperature at the nozzle exit
F	Propulsive thrust
x, y, z	Cartesian coordinate
X, Z	axial distance from the nozzle exit plane
$\boldsymbol{U}$	conserved vector quantities
u, v, w	velocity in x, y, z directions, respectively
V	velocity
δ	plate inclination angle

ρ density
β oblique shock angle
θ_w double-wedge deflector apex angle
γ ratio of specific heats

REFERENCES

1. Anon. Acoustic Loads Generated by the Propulsion System, Langley Research Centre, Hampton Virginia, USA, NASA SP-8072, 1971
2. https://youtu.be/gv4ClusLU2s?si=QOEdh96vhPM5sOR5, 30 November 2025
3. Evans, R. L. and Sparks, O. L., Launch Deflector Design Criteria and Their Applications to the Saturn C-1 deflector, George C. Marshall. Space Flight Center Huntsville, Alabama, NASA TN D 1275, 1963
4. Dordain, J. J., Firing-tests of a model of the Ariane launch vehicle, Acta Astronautica, 4(5 - 6), 1977, 727-748, https://doi.org/10.1016/0094-5765(77)90117-5.
5. Anon. Flame deflector design, standard for John F. Kennedy Space Center, NASA, KSC-STD-Z-0012B, June 20, 1990.
6. Allgood D., and Ahuja V. Computational plume modeling of conceptual ARES vehicle stage tests, 43rd AIAA/ASME/SAE/ASEE Joint Propulsion Conference & Exhibit. 2007-5708. DOI: 10.2514/6.2007-5708
7. Giordan, P., Fleury, P., and Guidon, L., Simulation of water injection into a rocket motor plume, 35th Joint Propulsion Conference and Exhibit, AIAA 1999-2517. https://doi.org/10.2514/6.1999-2517
8. Zhoua, Z., Zhangb, L. and Le, G., Numerical study for the flame deflector design of four-engine liquid rockets, Engineering Applications of Computational Fluid Mechanics. 2020, 14(1) 2020, 726–737 https://doi.org/10.1080/19942060.2020.1761453
9. Daniel, C. A., and Vineet, A., Computational plume modeling of conceptual ARES vehicle stage tests. Proceedings of the 43rd AIAA/ASME/SAE/ASEE Joint Propulsion Conference and Exhibit, Cincinnati, OH, USA. 2007 doi:10.2514/6.2007-5708
10. Hong, S. K., Park, S. O., Supersonic jet impingement Navier-Stokes computations for vertical launching system design applications. Journal of spacecraft and rockets, 2004, 41(5): 735-744. DOI: 10.2514/1.13077
11. Donaldson, C. duP., and Snedeker, R. S., A study of free jet impingement. Part 1. Mean property of free and impinging jet, Journal of Fluid Mechanics, 45(2), 1971, pp. 281-319.
12. Lamont, P. J., Hunt, B. L., The Impingement of underexpanded, axisymmetric jets on perpendicular and inclined flat plates, Journal of Fluid Mechanics, 100(3), 1980, 471–511. doi:10.1017/S0022112080001255
13. Tsuboi, N., Hayashi, K., Fujiwara, T., Arashi, K., and Kodama, M., Three-dimensional study of a supersonic jet impinging on a plate, in the proceedings of the 18th International Symposium on Space Technologies and Sciences, Kagoshima, Japan, Edited by H. Hirosawa, Part 1, 1992, pp. 805-810.
14. Kim, K. H., and Chang, K. S., Three-dimensional structure of a supersonic jet impinging on an inclined plate, Journal of Spacecraft and Rockets, 31(5) 1994, pp. 778-784. doi.org/10.2514/3.2651
15. Ding, J., Liu, Y., and He, H., Numerical study on the effect of rocket plume to the jet flow deflector in liquid rocket engine test stage, Third International Conference on Fluid Mechanics and Industrial Applications, IOP Conf. Series: Journal of Physics: Conf. Series 1300 (2019) 012052, IOP Publishing doi:10.1088/1742-6596/1300/1/01205
16. Nakai, Y., Fujimatsu, N., and Fujii, K., Experimental Study of underexpanded Supersonic Jet Impingement on an Inclined Flat Plate, AIAA Journal, 44(11), 2006, pp. 2691–2699. doi:10.2514/1.17514
17. Zhou, Z. T, Zhao, C. F., Lu, C. F., and Le, G. F., Numerical studies on four-engine rocket exhaust plume impinging on flame deflectors with afterburning, Defence Technology, 17 2021. 1207e1216, https://doi.org/10.1016/j.dt.2020.06.016
18. Jiang, C, Han, T., Gao, Z., Lee, C., A review of impinging jets during rocket launching. Prog Aero Sci. 2019;109. doi.org/10.1016/j.paerosci.2019.05.007
19. Mehta, R. C., Analysis of Supersonic Free Jets and Impinging Supersonic Jets, Simulation Modeling, Recent Advances, New Perspectives, and Applications, 2024 DOI: 10.5772/intechopen.100237
20. Mehta, R. C., CFD Simulations of Supersonic Jets Impinging on Axisymmetric and Double-Wedge Deflector of Satellite Launch Vehicle, Scholars Journal of Engineering and Technology, 13(9): 2025, 718-737 https://doi.org/10.36347/sjet.2025.v13i09.002
21. Wu J, Lin T, Luke, EA, Tong X, Cinnella P: Comprehensive numerical study of jet-flow impingement over flat plates. Journal of Spacecraft and Rockets. 2002; 39; 357-366. doi.org/10.2514/2.383
22. McIlroy K, and Fujii K., Computational analysis of supersonic underexpanded jets impinging on an inclined flat plate. AIAA Paper 2007-3859, 2007 https://doi.org/10.2514/6.2007-3859
23. Zhou, Z. T., Zhao, C. F., Lu, C. Y., and Le, G. G., Numerical studies on four-engine rocket exhaust plume impinging on flame deflectors with afterburning, Defence Technology 17, 2021 1207e1216, https://doi.org/10.1016/j.dt.2020.06.016
24. Brehm C., Sozer E., Moini-Yekta S., Housman J .A., Kiris C., Barad M. F., Vu B. T., and Parlied C. R., Computational prediction of pressure environment

in the flame trench with launch vehicles, AIAA 2013-2538. https://doi.org/10.2514/6.2013-2538
25. Akamine M., Okamoto K., Gee K. L., Neilsen T. B., Teramoto S., Okunuki T., and Tsutsumi S., Effect of nozzle-plate distance on acoustic phenomena from supersonic impinging jet, AIAA Journal, 56(1) 2018, https://doi.org/10.2514/1.J056504
26. Cobbald, T. J., The impingement of underexpanded, axisymmetric, rocket motor exhausts and cold jets on flat plates, Ph. D. thesis, University of Bristol, U.K., 1985.
27. Iwamoto, J., Impingement of underexpanded jets on a flat plate, ASME, Transactions, Journal of Fluids Engineering, vol. 112, 1990, p. 179-184.
28. Matsumura, Y. and Nishida, M., Numerical simulation of a supersonic free jet impingement, Space Technology and Science, 1992, pp. 679-683.
29. Hwayoung, O., Jungil, L., Hyungsik, U. and Hwanil, H., Numerical study for flame deflector design of a space launch vehicle. Advances in Space Research, 59(7), 2017, pp. 1833-1847 https://doi.org/10.1016/j.asr.2016.12.038
30. Kim, K. H., and Chang, K. S., Axisymmetric impingement of a hot jet on flat plate: equilibrium flow analysis of high temperature air, Shock Waves, 4, 1994, pp. 155-162. DOI: 10.1007/BF01417431
31. Prasad, J. K., Mehta, R. C., and Sreekanth, A. K., Impingement of supersonic jets on an axisymmetric deflector, AIAA Journal, 32(7) 1994, pp.1535-1538. https://doi.org/10.2514/3.12225
32. Mehta, R. C., Pandya, M. J. and Jayachandran, T., Euler calculations for diffuser flowfield, free jets and impingement jets, International Journal of Numerical Methods of Heat and Fluid Flows, 4(4), 1995, pp. 287-300. https://doi.org/10.1108/EUM0000000004066
33. Prasad, J. K., Mehta, R. C., and Sreekanth, A. K., Experimental study of over-expanded supersonic jet impingement on a double wedge deflector, The Aeronautical Journal, 97, (966),1993, pp. 209-214. https://doi.org/10.1017/S0001924000026245
34. Prasad, J. K., Mehta, R. C. and Sreekanth, A. K., Impingement of supersonic jets on a wedge and axisymmetric deflector, in the proceedings of 6th Asian Congress of Fluid Mechanics, Nanyang Technological University and National University of Singapore, Singapore, pp. 983-987, May 22-26, 1995.
35. Mehta, R. C., Numerical Simulation of Double Wedge Supersonic Jet Deflector, CFD journal, Japan Society of Computational Fluid Dynamics, 18(1) 2009, pp. 31-36
36. Mehta, R. C., Computational Fluid Dynamics Analysis of Underexpanded, Fully-Expanded and Overexpanded Supersonic Jets Emanating from a Convergent-Divergent Nozzle, Scholars Journal of Engineering and Technology, 13(7), 2025, 552-568, DOI: 10.36347/sjet. 2025.v13i07.008
37. Caron, C., Lauret, P., and Bastide, A., Machine Learning to speed up Computational Fluid Dynamics engineering simulations for built environments: A review, Building and Environment, 267, Part A, 2025, 112229, ISSN 0360-1323, https://doi.org/10.1016/j.buildenv.2024.112229.
38. Kordulla, W. and Vinokur, M., Efficient computation of volume in flow predictions, AIAA Journal, 21(4), 1983, 917-918 https://doi.org/10.2514/3.8174
39. Jameson, A., Schmidt, W., and Turkel, E., Numerical Simulation of Euler Equations by Finite Volume Methods Using Runge-Kutta Time Stepping Schemes, AIAA paper 81-1259, June 1981, https://doi.org/10.2514/6.1981-1259
40. Mehta, R. C., Multi-Block Structured Grid Generation for Computational Fluid Dynamics, Scholar Journal of Engineering and Technology, **5**(8), 2017, 87-219 DOI: 10.21276/sjet
41. Sasman, P. K. and Cresci, R. J., Compressible turbulent boundary layer with pressure gradient and heat transfer, AIAA Journal, 4(1), 1986, pp. 19-25, doi.org/10.2514/3.3378
42. Prasad, J. K., Mehta, R. C., and Sreekanth, A. K., Overexpanded supersonic jet impingement on double wedge deflector, Numerical Methods in Thermal Problems: Proceedings of the Sixth International Conference Held in Swansea, U.K., July, 1989, pp 951-958.
43. Prasad J. K. and Kutty C. S., Impingement on PSLV jet deflector cold flow simulation test results, Aerothermal Test Facilities, ATTF:07:85, Trivandrum, October, 1985
44. Handbook of Astronautical Engineering, Edited by H. H. Koelle, McGraw-Hill Book Co. Inc, USA, 1961.